PHYSICS OPEN

https://www.sciencedirect.com/journal/physics-open

Editor: Professor William A. Barletta, Massachusetts Institute of Technology (USA)

Accepted April 3rd, 2024.

COMPUTATION OF HYDROMAGNETIC TANGENT HYPERBOLIC NON-NEWTONIAN FLOW FROM A ROTATING NON-ISOTHERMAL CONE TO A NON-DARCY POROUS MEDIUM WITH THERMAL RADIATIVE FLUX

S. Abdul Gaffar[1*], O. Anwar Bég[2], S. Kuharat[2] and T.A. Bég[3]

[1]*Mathematics and Computing Section, Preparatory Studies Centre, University of Technology & Applied Sciences Salalah,* ***Oman****.*
Email: AbdulGaffar.Shaik@utas.edu.om
[2]*Multi-Physical Engineering Sciences Group, Mechanical Engineering Department, Corrosion and Coatings Lab, Room 3-08, SEE Building, University of Salford, Manchester, M54WT,* ***UK****.*
Email: *O.A.Beg@salford.ac.uk; S.Kuharat2@salford.ac.uk*
[3]*Engineering Mechanics Research, Israfil House, Dickenson Rd., Manchester, M13,* ***UK.***
Email: *tasveerabeg@gmail.com*
****Author for Correspondence: Email – abdulsgaffar0905@gmail.com***

ABSTRACT

A theoretical and numerical study is conducted on nonlinear, steady-state thermal convection boundary layer flow of a magnetized incompressible Tangent Hyperbolic non-Newtonian fluid from a rotating cone to a non-Darcy porous medium. Power-law variation in temperature on the cone surface is considered and thermal radiation heat transfer is also present. The Brinkman-Darcy-Forchheimer model is deployed for the porous medium. The study is motivated by rotational (spin) coating with new emerging magnetic rheological polymers, a process which often utilizes filtration media and high temperatures. The transformed non-dimensional conservation equations are solved numerically subject to physically appropriate boundary conditions using a second-order accurate implicit finite-difference Keller Box technique. The numerical code is validated with previous studies. Extensive visualization of axial, tangential velocity components and temperature distributions with variation in key parameters including Rosseland radiative number, Darcy number, Forchheimer number (non-Darcy inertial parameter), magnetic interaction parameter, tangent-hyperbolic non-Newtonian power-law index and Weissenberg (non-Newtonian) number is included. Additionally, axial and tangential (circumferential) skin friction and Nusselt number values are tabulated for variation in key control parameters. With increasing Weissenberg number, axial velocity is depleted near the cone surface, tangential velocity is suppressed throughout the boundary layer regime and temperature is strongly enhanced. Axial flow is strongly decelerated further from the cone surface with increasing tangent-hyperbolic power-law index and there is also a significant depletion in tangential (swirl) velocity. Temperature is however boosted throughout the boundary layer transverse to the cone surface with a rise in tangent-hyperbolic power-law index. Both tangential and axial velocity are suppressed with increment in magnetic interaction parameter whereas temperature and thermal boundary layer thickness are enhanced. With larger Darcy number (i.e. greater permeability), axial velocity is strongly increased near the cone surface with no tangible modification further from the cone; However tangential velocity is consistently elevated throughout the boundary layer with greater Darcy number whereas temperature is depleted. An increase in Forchheimer number substantially damps both axial and tangential velocity whereas it elevates temperature. Increasing radiative flux strongly energizes the magnetic polymer and elevates temperature but suppresses the axial and tangential velocities. With elevation in non-isothermal wall exponent, axial skin friction is suppressed whereas Nusselt number are elevated at the cone vertex. Further along the cone surface a similar response is observed but there is also a reduction in magnitudes of tangential skin friction.

KEYWORDS: *Non-Newtonian Tangent Hyperbolic fluid; Weissenberg number; Magnetic field; Electro-conductive polymers (ECPs); Darcy number; Forchheimer number; coating fluid mechanics.*

NOMENCLATURE

B_0	*Constant transverse (radial) magnetic field*
C_f	*Skin friction coefficient*
c_p	*Specific heat*
Da	*Darcy number*
f	*Non-dimensional steam function*
Fs	*Forchheimer number (second order inertial porous drag parameter)*
Gr_x	*Local Grashof number*
g	*Acceleration due to gravity*
k	*Thermal conductivity of the fluid*
K	*Thermal diffusivity*
k^*	*The mean absorption coefficient*
M	*Magnetic interaction parameter*
n	*Tangent hyperbolic non-Newtonian power law index*
m	*Wall non-isothermal surface temperature exponent (power law index)*
Nu	*Local Nusselt number (cone surface heat transfer rate)*
Pr	*Prandtl number*
q_r	*Radiative heat flux*
R	*Radiation-conduction parameter*

Re	*Local Reynolds number*
Ra	*Local Rayleigh number*
r	*Local radius of the cone*
T	*Temperature of the fluid*
u, v, w	*Non-dimensional velocity components along the x, y, z directions, respectively*
V	*Velocity vector*
We	*Weissenberg number (non-Newtonian parameter)*
x	*Stream wise coordinate*
y	*Transverse coordinate*

Greek

φ	*Semi-vertex angle of the cone*
α	*Thermal diffusivity*
β	*The coefficient of thermal expansion*
η	*The dimensionless radial coordinate*
μ	*Dynamic viscosity of magnetic polymer*
υ	*Kinematic viscosity of magnetic polymer*
θ	*Non-dimensional temperature*
ρ	*Density of magnetic polymer*
ξ	*Dimensionless tangential coordinate*
ψ	*Dimensionless stream function*
Γ	*Time-dependent material constant in tangent hyperbolic model*
Π	*Second invariant strain tensor*
Ω	*Angular velocity of cone*
Λ	*Inertial drag coefficient in non-Darcy drag force model*
σ^*	*Stefan-Boltzmann constant*

Subscripts

w	*Conditions at the wall (cone surface)*
∞	*Free stream conditions*

1. INTRODUCTION

Transport in porous media constitutes a rich area of modern engineering sciences. It involves the percolation of viscous fluids in complex permeable materials and arises in for example filtration design in ventilation systems [1], hybrid coatings for offshore platform structures [2], polymer manufacture [3] and metallic foam synthesis for aerospace systems [4] among many other technologies. Mathematical models of fluid dynamics in porous media have continued to evolve over the past century. Many different approaches have been developed including volume averaging, hierarchical porous media, reconstructed porous media, Serpenski carpets and even fractal approaches. The random heterogenous nature of porous media makes them complex to simulate precisely. Other approaches aim to build an approximate estimate of the net effect of solid fibers on transport of percolating fluids. Popular in this type of model is the drag force formulation. The most widely established such model is the Darcy model [5] which is generally valid for low Reynolds numbers or viscous-dominated flows. This model assumes that the pressure drop across the porous medium follows a linear relationship with the velocity of the fluid. However other models have emerged which generalize this approach to include nonlinear effects. These include the Darcy-Forchheimer model which incorporates a second order inertial drag force term to capture impedance effects at higher Reynolds numbers and the Darcy-Brinkman model which builds on a modification of the Navier-Stokes equations and includes the effects of vorticity diffusion. An interesting appraisal of such models has been given in Bağci [6]. Complex geometric effects in porous media may include tortuosity [7], anisotropic permeability, channelling, variable porosity and non-saturated zones in which all the pores are not occupied by the percolating fluids [8]. The drag force models however generally ignore these effects and have been deployed successfully in many isotropic, non-tortuous porous media hydrodynamics studies including biochar-based bipolar electrochemical flows in porous media [9], chemical filters [10], geological materials [11] and abiotic wall-cooled porous medium bioreactors [12]. Many studies have considered thermal convection and also mass diffusion in non-Darcy porous media. Mohanty *et al.* [13] deployed a Darcy-Forchheimer formulation to compute the free convection hybrid nanofluid flow past a stretching rotation disk with the Galerkin finite element numerical approach considering the effects of thermal radiation, exponential heat generation, viscous dissipation and activation energy. Mohanty *et al*. [14] used MATHLAB bvp4c method to study the entropy generation of Darcy-Forchheimer Hybrid nanofluid flow past infinite porous disk. They investigated the thermal Marangoni convection flow of nanomaterials MWCNT and MoS_2 embedded in base fluid water with conjugate effect of interfacial nanolayers. Venkatadri *et al.* [15] deployed a D2Q9-based Lattice Boltzmann Method to compute the natural convection hydromagnetic flow in differentially heated square enclosure containing a homogenous non-Darcian porous medium saturated with hybrid nanofluid (TiO_2/Cu–water). They showed that higher Forchheimer number and Hartmann magnetic number strongly damps circulation but intensifies heat transfer to the boundary. They also noted that larger Darcy number and Rayleigh number Hartmann magnetic number leads to stronger flow circulation and a reduction in heat transfer (lower Nusselt numbers at the hot wall). Overall, using a response surface methodology (RSM) approach they found that high Darcy number, low nanoparticle volumetric fraction, and low Hartmann number optimize heat transfer rates. Mohanty *et al.* [16] utilized a finite element method to compute the Cattaneo-Christov thermosolutal flux effects on nanofluid-saturated Darcy-Forchheimer porous media boundary layer flow along a moving needle considering the thermal radiation, Joule heating and viscous dissipation. Further studies of non-Darcy convection include Mohanty *et al.* [17] considered the irreversibility analysis of 3D Darcy-Forchheimer Casson hybrid nanofluid flow past a rotating disk using the Runge-Kuttal-Fehlberg based shooting technique. Bég *et al.* [18] used a variational finite element method to compute the thermal convection boundary layer flow of a third grade Reiner-Rivlin viscoelastic fluid from an isothermal wall to a non-Darcian permeable medium. They noted that strong flow acceleration is achieved with larger Darcy numbers (greater permeability) whereas significant flow deceleration (thicker momentum boundary layers) are computed with elevation in Forchheimer (second order inertial drag) number.

The above studies did not consider rotational effects. In polymer spin coating processes in chemical engineering, an external coating can be deposited precisely on a revolving geometry. The centrifugal forces generated by the rotation of the body being coated may be tuned to produce improved quality of the surface finishing. The spreading coating exhibits an external boundary layer nature, and the boundary layer grows radially outwards. This process has been increasingly adopted in recent years for synthesizing thin polymeric coatings. Often spin coating is accompanied with thermal convection heat transfer. Porous media can be deployed external to the rotating body (substrate) to achieve further manipulation of the coating characteristics. Several investigators have therefore examined the boundary layer convection from rotating bodies to non-Darcian porous media. Kumar *et al.* [19] used a Runge-Kutta method to simulate the impact of activation energy on viscoplastic (Casson) fluid from a rotating disk which moves upwards/downwards to a Darcy–Forchheimer porous medium saturated with a Graphene oxide/Titanium dioxide-Ethylene glycol nanofluid. They noted that the upward and downward motion of the disk exerts similar effects to that of the injection/suction through the wall and that in both cases Forchheimer drag decelerates the radial flow but enhances tangential flow whereas increasing Darcy number exerts the opposite effect. Saleh *et al.* [20] used the Marker and Cell (MAC) method to compute the free convection heat transfer in a rotating, differentially heated enclosure containing a Forchheimer–Brinkman-extended Darcian porous medium. They examined the impact of porosity, Darcy number and Taylor number (ratio of Centrifugal "forces" due to rotation relative to viscous forces), for the scenario where centrifugal force is of lower magnitude than Coriolis force. They noted that the circulation is strongly damped with greater Forchheimer effect, Nusselt number is boosted with greater porosity and Darcy number whereas it is depleted with greater Taylor number, and that larger porosities generate weaker vortex strengths when thermal buoyancy force exceeds the Coriolis force. Umavathi and Bég [21] used MATLAB software to compute the von Karman swirling slip flow of a nanofluid from a rotating disk adjacent to a non-Darcy porous medium with the Darcy–Forchheimer–Brinkman and Buongirono two-component nanoscale models. They noted that radial, axial and tangential flow deceleration is produced with increasing Forchheimer inertial drag and velocity wall slip, whereas acceleration is generated with increasing permeability (decreasing inverse Darcy parameter). They also observed that temperatures and nanoparticle concentrations are suppressed with increasing Forchheimer inertial parameter, Schmidt number and Prandtl number whereas they are elevated with thermophoresis and Brownian motion parameters. Further investigations of transport from rotating bodies to porous media include Bég *et al.* [22] who consider anisotropic permeability effects from a revolving cone using MAPLE quadrature.

In high temperature coating operations, radiative heat transfer can arise. This mode of heat transfer is much more complex than thermal conduction and thermal convection. It is influenced by many factors including optical density of the coating and many mathematical models are available for simulating radiative flux effects. These include the Schuster-Schwartzchild two flux model, Traugott differential flux model, Chandrasekhar discrete ordinates model (DOM) etc [23]. Many different technologies have used radiative high temperature processing including thermal barrier coatings for gas turbine blades [24], microalgae photobioreactors [25], textile façade systems [26], pulverized coal combustors [27] and thermochromic de/anti-icing coating systems [28]. While computational fluid dynamics (CFD) tools have been deployed with for example Chandrasekhar discrete ordinates model (DOM) in these applications, they require very highly intensive hardware and long compilation times due to the complexity of the integro-differential radiative heat transfer equation. A much more pragmatic approach popular in engineering sciences is the use of an algebraic flux model of which the Rosseland diffusion approximation is probably the most widely deployed. This model is particularly suitable for boundary layer flows as it involves inclusion of an augmented term for radiative flux in the energy equation rather than a separate radiative heat transfer equation. While limited to optically thick fluids, Rosseland's model has been implemented extensively in recent years in both purely fluid regimes and also porous media transport problems. Venkatadri *et al.* [29] used a finite difference method, Hooman's method of energy flux vectors (EFVs) and the Rosseland flux model to simulate and visualize the steady laminar free convection-radiation heat transfer in a triangular enclosure containing a Darcy-Brinkman variable porosity medium. They observed that increasing Darcy number (permeability) boosts the convective heat transfer and intensifies EFV patterns, larger Rayleigh number intensifies circulation and greater radiative flux increases isotherm magnitudes whereas an increment in porosity suppresses average Nusselt number. Mohanty *et al.* [30] used a Galerkin finite element method to simulate Cattaneo-Christov heat flux on the interfacial nanolayer thickness with MWCNT and Au-embedded water- based hybrid nanofluid from a spinning sphere. Further studies include Sarangi *et al.* [31] investigated the impacts of second order slip on the Bodewadt flow and heat transfer flows of radiative and dissipative ternary composite nanofluid from a stretching rotating disk, in addition to entropy analysis to scrutinize the thermal efficiency. Debashis *et al.*, [32] used a homotopy method to analyze the flow and thermal behavior of a cross-ternary *SWCNT*, *MWCNT*, and *GO* nanoparticles composite water-based ternary hybrid nanofluid past a stretched cylinder. They included Joule heating and non-linear thermal radiation with wall boundary convective conditions.

The above investigations have generally neglected electrical conductivity properties of coating fluids. In recent years, however, many new complex functional magnetic polymers have been developed for a range of technological applications. These are known as electro-conductive polymers (ECPs) and they feature both magnetohydrodynamic (MHD) and rheological characteristics. These smart materials can be finetuned to achieve improved performance which is generated via embedding metallic conducting particles in the coating melt which incur electro-active phases of the material under the action of an external magnetic field. To simulate accurately the fluid dynamics of such polymers, both viscous magnetofluid dynamics [33, 34] and rheological modelling [35] are required. Magnetic polymers have found extensive applications in thin film deposition in nuclear reactor ducts [36], MHD generators [37], biomedical components [38] and chemical engineering self-healing surface protection using orderly distributed microcapsules (ODM), linseed oil (LO) and magnetic benzotriazole (BTA) which enhance defect sealing and corrosion inhibition. Many complex materials have therefore been developed including cobalt based thin magnetic films [39], nickel/aluminium electroconductive foam coatings [40] and iron oxide magnetic nano-coatings [41]. A number of studies of MHD coating flows have also appeared in parallel to the extensive experimental studies reported. These investigations have also featured radiative heat transfer (important in high temperature surface deposition) and porous medium physics (deployed for filtration and purification purposes). Bég *et al.* [42] used a variational finite element method code (*MAGNETO-FEM*) and also a network simulation method code (*MAG-PSPICE*) to simulate the effects of thermal radiation and transverse magnetic field on reactive coating boundary layer flow on a substrate with Soret and Dufour diffusion and viscous heating effects. They showed that strong elevation in velocity is observed with increasing thermal radiative flux and Soret number whereas the flow is retarded (thicker momentum boundary layers) with greater wall suction, magnetic field and Prandtl number. They also noted that thermal boundary layer thickness is enhanced with magnetic field, radiative flux, Dufour number and Eckert number whereas species concentration is boosted with Soret number and generative chemical reaction. Thumma *et al.* [43] employed a finite element method to study the hydromagnetic nano-polymer coating flow deposition on an oscillating tilted substrate with radiative flux using the Rosseland model. They considered copper/alumina-aqueous coatings and noted that higher radiative heat transfer strongly energizes the coating flow and increases thermal boundary layer thickness. Further studies include Prasad *et al*. [44] (who considered non-Darcian effects). Rotating MHD coating flows have also received some attention. These investigations combine the use of an external transverse magnetic field (static or oscillating) and centrifugal body forces to produce enhanced control and consistency of the functional coating. Important studies in this regard include Carreri *et al.* [47] who considered deposition on a revolving cylindrical cathode and Moreira *et al.*, [48] who utilized strong magnetic fields for fabrication of thin-film coatings over large spinning areas with smooth and homogeneous surfaces. Kumari and Nath [49] described numerical simulations of the magnetohydrodynamic unsteady boundary layer flow on a revolving spherical substrate. They used both asymptotic and numerical methods to consider the coating fluid and the sphere are impulsively rotated with dissimilar spin velocities either in the same direction or in opposite directions. Further investigations include Zohra *et al.* [50] (who considered bioconvection magnetic slip nanofluid flow from a spinning cone) and Shah *et al.* [51] (on radiative heat flux effects on magnetic Carbon nanotubes coatings on a rotating stretching sheet). These studies showed that optimal coating and heat transfer rates can be achieved with careful combinations of radiative flux and centrifugal force.

The focus of the present study is to investigate the effects of thermal radiative flux on steady laminar convection boundary layer flow and heat transfer in magnetized tangent hyperbolic non-Newtonian coating flow external to a spinning cone in a Darcy-Brinkman-Forchheimer porous medium with power-law variation in wall (cone surface) temperature. *The novelty of the present study is therefore the simultaneous consideration of tangent hyperbolic rheology, non-isothermal wall behaviour, thermal radiation, magnetohydrodynamics and non-Darcy porous effects*. These effects have to the authors' knowledge not been considered thus far in the scientific literature. The

Brinkman-Darcy-Forchheimer model is deployed for the porous medium which is assumed to be isotopic and homogenous. Rosseland's diffusion flux approximation [52, 53] is employed for the radiative heat transfer. The transformed non-dimensional conservation equations are solved numerically subject to physically appropriate boundary conditions using a second-order accurate implicit finite-difference Keller Box technique [54]. The numerical code is validated with previous studies. Comprehensive graphs are presented for the impact of key thermophysical, hydrodynamic and non-Newtonian parameters namely the Rosseland radiative number, Darcy number, Forchheimer number (non-Darcy inertial parameter), magnetic interaction parameter, tangent-hyperbolic non-Newtonian power-law index, non-isothermal power law index and Weissenberg (non-Newtonian) number on axial, tangential velocity components and temperature distributions with is included. Additionally, axial and tangential (circumferential) skin friction and Nusselt number values are tabulated for variation in selected key control parameters. The present simulations will be beneficial for industrial coating designers in optimizing thermal processes in magnetic polymer spin coating with porous media.

2. HYDROMAGNETIC SPINNING CONE RHEOLOGICAL COATING MODEL

The regime under consideration comprises the steady, laminar, axisymmetric, electrically conducting, incompressible radiative-convective boundary layer flow of a tangent hyperbolic magnetic polymer from a steadily rotating inverted vertical cone with a non-isothermal (variable wall temperature) external surface to a non-Darcy isotropic homogenous porous medium. This system is depicted in **Fig. 1.** in an (x, y, z) coordinate system. The vertical cone spins at a constant angular velocity, Ω, around its axis of symmetry. Fluid friction causes a circumferential velocity, w, of fluid elements, which are also subjected to a centrifugal force causing the radial velocity, v. By virtue of mass conservation, the outward-moving fluid is being replaced by fluid eventually flowing along the cone surface with velocity u. An external static uniform magnetic field, B_0 acts transverse to the cone surface. The surface of the cone is sustained at a variable temperature proportional to the power of the distance along the cone from the vertex (x) i.e., $T_w\left(x\right)=T_\infty+ax^m$, where a and m are constants. Gravitational acceleration, $\boldsymbol{g}$, acts downwards. The magnetic Reynolds number is assumed to be small enough to neglect magnetic induction effects since the magnetic field is not distorted. The Brinkman-Darcy-Forchheimer model is deployed for the porous medium. Rosseland's diffusion flux approximation [52, 53] is employed for the radiative heat transfer and the magnetic polymer is assumed to be optically thick.

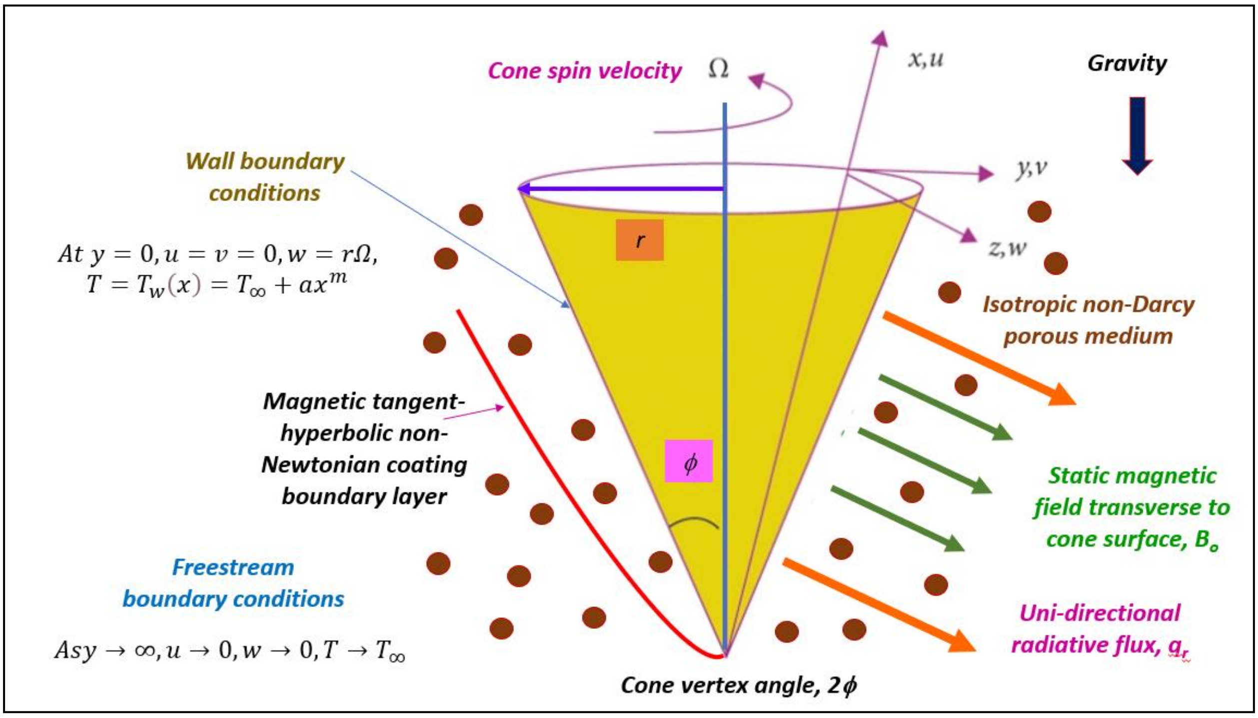

Fig. 1 Magnetic non-Newtonian coating with radiative heat transfer from a rotating cone

The viscoelasticity and pseudoplasticity of the magnetic polymer to be investigated is studied with the tangent hyperbolic non-Newtonian model. The associated Cauchy stress tensor for the coating fluid can be shown to take the form [55]:

$$\bar{\tau} = \left[\mu_\infty + \left(\mu_0 + \mu_\infty \right) \tanh \left(\Gamma \bar{\dot{\gamma}} \right)^n \right] \bar{\dot{\gamma}} \qquad (1)$$

where $\bar{\tau}$ is extra stress tensor, μ_∞ is the infinite shear rate viscosity, μ_0 is the zero shear rate viscosity, Γ is the time dependent material constant, m is the rheological power law index i.e. flow behaviour index and $\bar{\dot{\gamma}}$ is defined as:

$$\bar{\dot{\gamma}} = \sqrt{\frac{1}{2} \sum_i \sum_j \bar{\dot{\gamma}}_{ij} \bar{\dot{\gamma}}_{ji}} = \sqrt{\frac{1}{2} \Pi} \qquad (2)$$

Here $\Pi = \frac{1}{2} tr\left(gradV + \left(gradV \right)^T \right)^2$. We consider Eqn. (1), for the case when $\mu_\infty = 0$ as it is not possible to simulate the flow problem for the infinite shear rate viscosity and for shear thinning effects so $\Gamma \bar{\dot{\gamma}} < 1$. Then Eqn. (1) takes the form:

$$\bar{\tau} = \mu_0\left[\left(\Gamma\dot{\bar{\gamma}}\right)^n\right]\dot{\bar{\gamma}} = \mu_0\left[\left(1+\Gamma\dot{\bar{\gamma}}-1\right)^n\right]\dot{\bar{\gamma}}$$
$$= \mu_0\left[1+n\left(\Gamma\dot{\bar{\gamma}}-1\right)\right]\dot{\bar{\gamma}} \qquad (3)$$

The appropriate electromagnetic equations are as follows [34]:

Maxwell Electromagnetic Equations:

$$\vec{\nabla}\cdot\mathbf{B} = \mu_e J \qquad (4)$$

$$\vec{\nabla}\cdot\mathbf{E} = -\frac{\partial\mathbf{B}}{\partial t} \qquad (5)$$

$$\vec{\nabla}\cdot\mathbf{J} \neq 0 \qquad (6)$$

$$\vec{\nabla}\cdot\mathbf{B} = 0 \qquad (7)$$

Here ***q*** is the velocity vector $\left(\bar{u},\bar{v},\bar{w}\right)$, ***J*** = *(J*$_r$*, J*$_\theta$*, J*$_z$*)* is electrical current density vector, *B* is the magnetic field vector, ***E*** is the electrical field vector, σ is electrical conductivity of the magnetic polymer. Furthermore, μ_e *is the magnetic permeability* of the fluid. Since there exists no applied or polarization voltage on the magnetic polymer flow field, and the cone surface is electrically insulated, the electric field vector vanishes i. e. ***E*** = 0. Under these approximations, and invoking the appropriate terms from the tangent hyperbolic model eqn. (3), the boundary layer equations under the linear Boussinesq approximation may be written by extending the model of Abo-Eldahab and Elaziz [56] to include non-Darcy effects:

$$\frac{\partial(ru)}{\partial x}+\frac{\partial(rv)}{\partial y}=0 \qquad (8)$$

$$u\frac{\partial u}{\partial x}+v\frac{\partial u}{\partial y}-\frac{w^2}{x}=\nu(1-n)\frac{\partial^2 u}{\partial y^2}+\sqrt{2}\,n\nu\Gamma\left(\frac{\partial u}{\partial y}\right)\frac{\partial^2 u}{\partial y^2}+g\beta(T-T_\infty)\cos\varphi-\left(\frac{\sigma B_0^2}{\rho}+\frac{\nu}{K}\right)u-\Lambda u^2$$
$$(9)$$

$$u\frac{\partial w}{\partial x}+v\frac{\partial w}{\partial y}+\frac{u\,w}{x}=\nu(1-n)\frac{\partial^2 w}{\partial y^2}+\sqrt{2}\,n\nu\Gamma\left(\frac{\partial w}{\partial y}\right)\frac{\partial^2 w}{\partial y^2}-\left(\frac{\sigma B_0^2}{\rho}+\frac{\nu}{K}\right)w-\Lambda w^2 \qquad (10)$$

$$u\frac{\partial T}{\partial x}+v\frac{\partial T}{\partial y}=\frac{k}{\rho c_p}\frac{\partial^2 T}{\partial y^2}-\frac{1}{\rho c_p}\frac{\partial q_r}{\partial y} \qquad (11)$$

The corresponding boundary conditions are:

$$At\ y=0, u=v=0, w=r\Omega, T=T_w(x)=T_\infty+ax^m$$

$$As\ \ y \to \infty, u \to 0, w \to 0, T \to T_\infty \tag{12}$$

The Rosseland algebraic diffusion approximation is deployed for the radiative heat flux q_r [43, 52]:

$$q_r = -\frac{4\sigma^*}{3k^*}\frac{\partial T^4}{\partial y} \tag{13}$$

Implementing the Taylor series approximation for T^4, we have:

$$T^4 \cong 4T_\infty^3 T - 3T_\infty^4 \tag{14}$$

Using Eqn. (14) in Eqn. (11), yields the modified version of the energy (thermal boundary layer) eqn, viz:

$$u\frac{\partial T}{\partial x} + v\frac{\partial T}{\partial y} = \left(1+R\right)\frac{\partial^2 T}{\partial y^2} \tag{15}$$

Here $R = \dfrac{16\sigma * T_\infty^3}{3k\,k*}$ and represents the Rosseland-Boltzmann radiative parameter (also known as Stark number). The dimensional stream function ψ is defined by the Cauchy-Riemann equations, $ru = \dfrac{\partial \psi}{\partial y}$ and $rv = -\dfrac{\partial \psi}{\partial x}$, and therefore, the continuity equation (8) is automatically satisfied. Here the *local radius* is defined as $r\left(x\right) = x\sin\varphi$.

In order to render the governing equations and the boundary conditions in dimensionless form, the following non-dimensional quantities are introduced.

$$\begin{gathered}\xi = \frac{\zeta}{1+\zeta}, \quad \eta = \frac{y}{x}\chi, \quad \psi = r\alpha\chi f, \quad g\left(\xi,\eta\right) = \frac{w}{r\Omega}, \quad \theta\left(\xi,\eta\right) = \frac{T-T_\infty}{T_w - T_\infty}, \\ \chi = \frac{\mathrm{Re}^{1/2}}{\xi}, \quad \zeta = \frac{\mathrm{Re}^{1/2}}{\mathrm{R}\,a^{1/4}}, \quad \mathrm{Re} = \frac{x^2\Omega\sin\varphi}{\nu}, \quad Ra = \frac{g\beta\left(T_w - T_\infty\right)x^3\cos\varphi}{\alpha\nu}\end{gathered} \tag{16}$$

Invoking the scaling transformations defined in eqn. (16), the boundary layer eqns. (9), (10) and (15) are reduced to the following coupled, nonlinear, *dimensionless axial and tangential linear momentum and thermal* partial differential boundary layer equations in a (ξ, η) coordinate system:

$$\begin{gathered}\Pr\left(1-n\right)f\,''' + \left(2 - \frac{\left(1-\xi\right)\left(1-m\right)}{4}\right)f\ f\,'' + nW_e f\,''\ f\,''' + \Pr\left(1-\xi\right)^4\theta + \Pr^2\xi^4 g^2 \\ -\left(1 - \frac{\left(1-\xi\right)\left(1-m\right)}{2} + Fs\,\xi\right)f\,'^2 \ - \Pr\xi^2\left(M + \frac{1}{Da}\right)f\,' = \xi\left(1-\xi\right)\left(\frac{1-m}{4}\right)\left(f\,'\frac{\partial f\,'}{\partial\xi} - f\,''\frac{\partial f}{\partial\xi}\right)\end{gathered} \tag{17}$$

$$\Pr\left(1-n\right)g''+\Pr nW_e\,\xi^2 g'g''+\left(2-\frac{\left(1-\xi\right)\left(1-m\right)}{4}\right)fg'-2gf'-\Pr\xi^2\left(M+\frac{1}{Da}\right)g$$
$$-\Pr\,Fs\,\xi^3 g^2=\xi\left(1-\xi\right)\left(\frac{1-m}{4}\right)\left(f'\frac{\partial g}{\partial\xi}-g'\frac{\partial f}{\partial\xi}\right) \quad (18)$$

$$\theta''\left(1+R\right)+\left(2-\frac{\left(1-\xi\right)\left(1-m\right)}{4}\right)f\theta'-m\theta f'=\xi\left(1-\xi\right)\left(\frac{1-m}{4}\right)\left(f'\frac{\partial\theta}{\partial\xi}-\theta'\frac{\partial f}{\partial\xi}\right) \quad (19)$$

The transformed dimensionless wall and free stream boundary conditions (12) by virtue of eqn. (16) emerge as:

$$\begin{array}{lllll} At\quad \eta=0, & f=0, & f'=0, & g=1, & \theta=1 \\ As\quad \eta\to\infty, & f'\to 0, & g\to 0, & \theta\to 0 & \end{array} \quad (20)$$

In eqns. (17)-(19), primes denote the differentiation with respect to transverse coordinate, η, $\Pr=\frac{\nu}{\alpha}$ is Prandtl number, $W_e=\frac{\sqrt{2}\,\nu\,\Gamma\,\chi^3}{x^2}$ is Weissenberg number, $M=\frac{\sigma B_0^2}{\rho\Omega\sin\varphi}$ is magnetic interaction parameter (ratio of Lorentzian magnetic body force to rotational body force), $Da=\frac{K\,\Omega\sin\varphi}{\nu}$ is a modified Darcy number and $Fs=\Lambda\chi\sqrt{\frac{\nu}{\Omega\sin\varphi}}$ is a modified Forchheimer inertial porous drag number. All these parameters are defined in the notation section. The skin-friction coefficient components in the axial and tangential (circumferential) directions (shear stresses at the cone surface) and Nusselt number (heat transfer rate at the cone surface), subject to the scaling transformations in eqn. (16) are readily obtained as follows:

$$C_{wx}=\left(1-n\right)f''(\xi,0)+\frac{n}{2\Pr}W_e\left(f''(\xi,0)\right)^2 \quad (21)$$

$$C_{wz}=\left(1-n\right)\Pr\xi^2 g'\left(\xi,0\right)+\frac{\Pr n}{2}W_e\xi^4\left(g'\left(\xi,0\right)\right)^2 \quad (22)$$

$$Nu=-\theta'(\xi,0) \quad (23)$$

The location, *ξ~ 0 i. cone vertex*, corresponds to the vicinity of the lower stagnation point on the cone. For this scenario, the model defined by eqns. (17) – (19) reduces to an ordinary differential boundary value problem:

$$\Pr\left(1-n\right)f'''+nW_e f''f'''+\left(\frac{7+m}{4}\right)f\,f''-\left(\frac{1+m}{2}\right)f'^2+\Pr\theta=0 \quad (24)$$

$$\Pr\left(1-n\right)g''+\left(\frac{7+m}{4}\right)fg'-2gf'=0 \quad (25)$$

$$\theta''(1+R)+\left(\frac{7+m}{4}\right)f\theta'-mf'\theta=0 \tag{26}$$

3. COMPUTATIONAL KELLER BOX SOLUTION AND VALIDATION

The general model defined by eqns. (17) - (19) with associated boundary conditions (20) for *radiative convective magnetic polymer swirling flow from a revolving non-isothermal cone to a non-Darcian porous medium* is solved using the unconditionally stable second order accurate implicit finite difference technique known as the Keller-box finite difference method [54] which can accommodate arbitrary spacing and possesses excellent extrapolation features. An in-house code has been developed in MATLAB symbolic software environment.

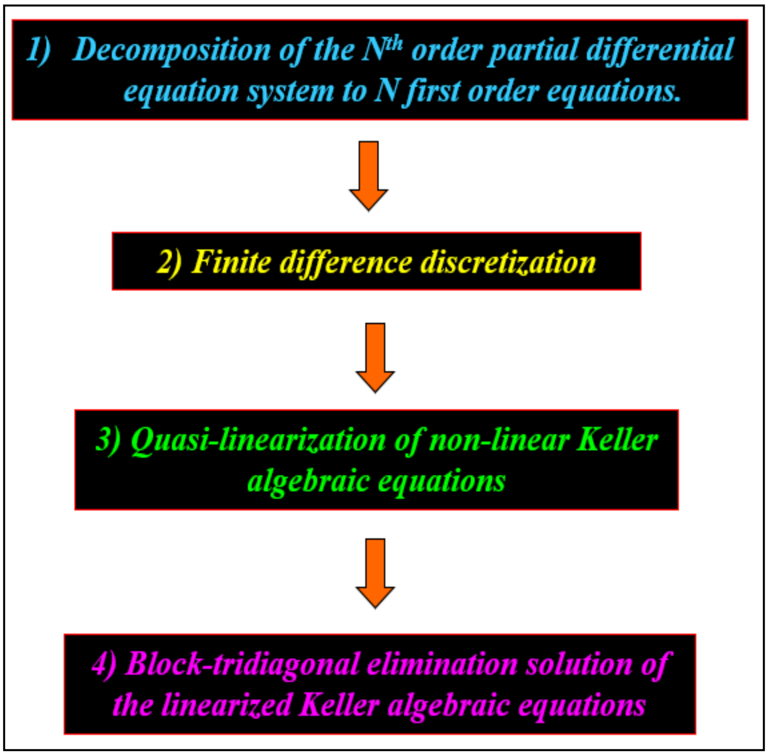

Fig. 2: Stages involved in the Keller box implicit finite difference scheme.

Stage 1: Decomposition of $\mathbf{N^{th}}$ **order partial differential equation system to** ***N*** **first order equations**

Equations (17) – (19) subject to the boundary conditions (20) are first cast as a multiple system of first order differential equations. New dependent variables are introduced:

$$u(x,y)=f',\; v(x,y)=f'',\; s(x,y)=\theta,\; t(x,y)=\theta' \tag{27}$$

$$f'=u \tag{28}$$

$$u'=v \tag{29}$$

$$g' = p \tag{30}$$

$$s' = t \tag{31}$$

$$\begin{aligned}&\Pr\left(1-n\right)v' + \left(2 - \frac{\left(1-\xi\right)\left(1-m\right)}{4}\right) f\, v + nW_e v\, v' + \Pr\left(1-\xi\right)^4 s + \Pr^2 \xi^4 g^2 \\ &\quad -\left(1 - \frac{\left(1-\xi\right)\left(1-m\right)}{2} + Fs\,\xi\right) u^2 - \Pr \xi^2 \left(M + \frac{1}{Da}\right) u = \xi\left(1-\xi\right)\left(\frac{1-m}{4}\right)\left(u\frac{\partial u}{\partial \xi} - v\frac{\partial f}{\partial \xi}\right)\end{aligned} \tag{32}$$

$$\begin{aligned}&\Pr\left(1-n\right) p' + \Pr nW_e \xi^2 p\, p' + \left(2 - \frac{\left(1-\xi\right)\left(1-m\right)}{4}\right) f\; p - 2g\,u \\ &\quad - \Pr \xi^2 \left(M + \frac{1}{Da}\right) g - \Pr\; Fs\,\xi^3 g^2 = \xi\left(1-\xi\right)\left(\frac{1-m}{4}\right)\left(u\frac{\partial g}{\partial \xi} - p\frac{\partial f}{\partial \xi}\right)\end{aligned} \tag{33}$$

$$t'\left(1+R\right) + \left(2 - \frac{\left(1-\xi\right)\left(1-m\right)}{4}\right) ft - m\left(su\right) = \xi\left(1-\xi\right)\left(\frac{1-m}{4}\right)\left(u\frac{\partial s}{\partial \xi} - t\frac{\partial f}{\partial \xi}\right) \tag{34}$$

where primes denote differentiation with respect to η. In terms of the dependent variables, the boundary conditions become:

$$\begin{aligned}&At \quad \eta = 0, \quad f = 0, \quad u = 0, \quad g = 1; \quad s = 1 \\ &As \quad \eta \to \infty, \quad u \to 0, \quad g \to 0, \quad s \to 0\end{aligned} \tag{35}$$

Step 2: Finite Difference Discretization

A two-dimensional computational grid is imposed on the ξ-η plane as sketched in **Fig. 3.** The stepping process is defined by:

$$\begin{aligned}&\eta_0 = 0, \quad \eta_j = \eta_{j-1} + h_j, \quad j = 1,2,...,J, \quad \eta_j = \eta_\infty \\ &\xi^0 = 0, \quad \xi^n = \xi^{n-1} + k_n, \quad n = 1,2,...,N\end{aligned} \tag{36}$$

where k_n is the $\Delta\xi$ - spacing and h_j is the $\Delta\eta$ - spacing. If g_j^n denotes the value of any variable at $\left(\eta_j, \xi^n\right)$, then the variables and derivatives of Equations (28) – (34) at $\left(\eta_{j-1/2}, \xi^{n-1/2}\right)$ are replaced by:

$$g_{j-1/2}^{n-1/2} = \frac{1}{4}\left(g_j^n + g_{j-1}^n + g_j^{n-1} + g_{j-1}^{n-1}\right) \tag{37}$$

$$\left(\frac{\partial g}{\partial \eta}\right)_{j-1/2}^{n-1/2} = \frac{1}{2h_j}\left(g_j^n - g_{j-1}^n + g_j^{n-1} - g_{j-1}^{n-1}\right) \tag{38}$$

$$\left(\frac{\partial g}{\partial \xi}\right)_{j-1/2}^{n-1/2} = \frac{1}{2k^n}\left(g_j^n - g_{j-1}^n + g_j^{n-1} - g_{j-1}^{n-1}\right) \tag{39}$$

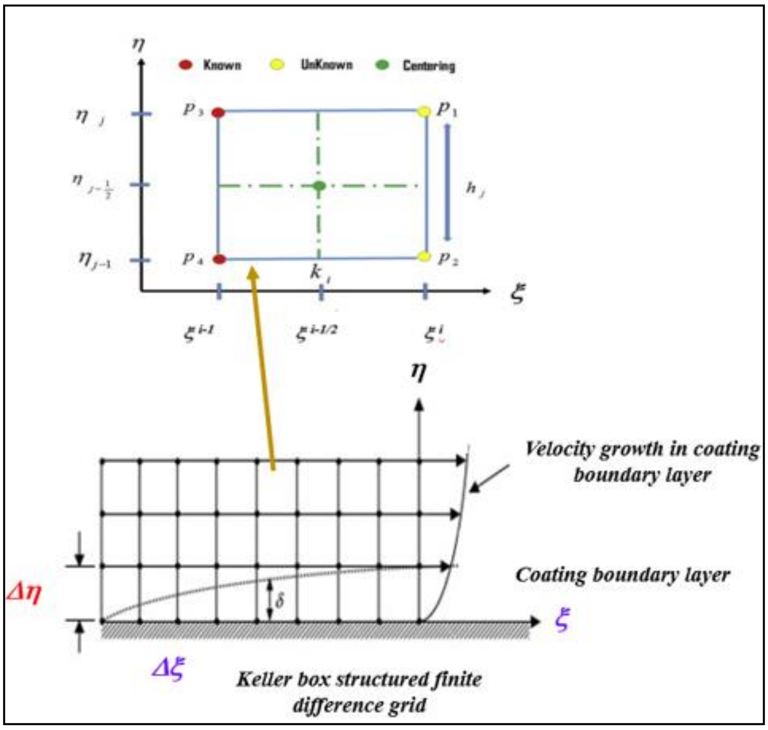

Fig. 3 Keller box computational cell and boundary layer meshing procedure

The resulting finite - difference approximation of equations (28) – (34) for the mid - point $\left(\eta_{j-1/2},\, \xi^{n}\right)$, are:

$$h_j^{-1}\left(f_j^n - f_{j-1}^n\right) = u_{j-1/2}^n \tag{40}$$

$$h_j^{-1}\left(u_j^n - u_{j-1}^n\right) = v_{j-1/2}^n \tag{41}$$

$$h_j^{-1}\left(g_j^n - g_{j-1}^n\right) = p_{j-1/2}^n \tag{42}$$

$$h_j^{-1}\left(s_j^n - s_{j-1}^n\right) = t_{j-1/2}^n \tag{43}$$

$$\begin{aligned}
&\Pr(1-n)\left(v_j - v_{j-1}\right) + \left(2 - \frac{(1-\xi)(1-m)}{4} + \frac{\alpha(1-\alpha)(1-m)}{4}\right)\frac{h_j}{4}\left(f_j + f_{j-1}\right)\left(v_j + v_{j-1}\right) \\
&+ \frac{nWe}{2}\left(v_j + v_{j-1}\right)\left(v_j - v_{j-1}\right) - \left(1 - \frac{(1-\xi)(1-m)}{2} + \frac{\alpha(1-\alpha)(1-m)}{4} + Fs\,\xi\right)\frac{h_j}{4}\left(u_j + u_{j-1}\right)^2 \\
&+ \Pr(1-\xi)^4\,\frac{h_j}{2}\left(s_j + s_{j-1}\right) + \Pr^2\xi^4\,\frac{h_j}{4}\left(g_j + g_{j-1}\right)^2 - \Pr\xi^2\left(M + \frac{1}{Da}\right)\frac{h_j}{2}\left(u_j + u_{j-1}\right) \\
&- \frac{\alpha(1-\alpha)(1-m)h_j}{8}\, f_{j-1/2}^{n-1}\left(v_j + v_{j-1}\right) + \frac{\alpha(1-\alpha)(1-m)h_j}{8}\, v_{j-1/2}^{n-1}\left(f_j + f_{j-1}\right) = \left[R_1\right]_{j-/12}^{n-1}
\end{aligned} \tag{44}$$

$$\begin{aligned}
&\Pr(1-n)\left(p_j-p_{j-1}\right)+\frac{\Pr}{2}nW_e\,\xi^2\left(p_j+p_{j-1}\right)\left(p_j-p_{j-1}\right)-\Pr\xi^2\left(M+\frac{1}{Da}\right)\frac{h_j}{2}\left(g_j+g_{j-1}\right)\\
&+\left(2-\frac{(1-\xi)(1-m)}{4}+\frac{\alpha(1-\alpha)(1-m)}{4}\right)\frac{h_j}{4}\left(f_j+f_{j-1}\right)\left(p_j+p_{j-1}\right)-\Pr\,Fs\,\xi^3\,\frac{h_j}{4}\left(g_j+g_{j-1}\right)^2\\
&-\left(2+\frac{\alpha(1-\alpha)(1-m)}{4}\right)\frac{h_j}{4}\left(g_j+g_{j-1}\right)\left(u_j+u_{j-1}\right)\\
&+\frac{\alpha(1-\alpha)(1-m)h_j}{8}\begin{pmatrix} g_{j-1/2}^{n-1}\left(u_j+u_{j-1}\right)-u_{j-1/2}^{n-1}\left(g_j+g_{j-1}\right)\\ -f_{j-1/2}^{n-1}\left(p_j+p_{j-1}\right)+p_{j-1/2}^{n-1}\left(f_j+f_{j-1}\right)\end{pmatrix}=\left[R_2\right]_{j-/12}^{n-1}
\end{aligned}\tag{45}$$

$$\begin{aligned}
&(1+R)\left(t_j-t_{j-1}\right)+\left(2-\frac{(1-\xi)(1-m)}{4}+\frac{\alpha(1-\alpha)(1-m)}{4}\right)\frac{h_j}{4}\left(f_j+f_{j-1}\right)\left(t_j+t_{j-1}\right)\\
&-\left(m+\frac{\alpha(1-\alpha)(1-m)}{4}\right)\frac{h_j}{4}\left(s_j+s_{j-1}\right)\left(u_j+u_{j-1}\right)\\
&+\frac{\alpha(1-\alpha)(1-m)h_j}{8}\left(s_{j-1/2}^{n-1}\left(u_j+u_{j-1}\right)-u_{j-1/2}^{n-1}\left(s_j+s_{j-1}\right)-f_{j-1/2}^{n-1}\left(t_j+t_{j-1}\right)+t_{j-1/2}^{n-1}\left(f_j+f_{j-1}\right)\right)\\
&=\left[R_3\right]_{j-/12}^{n-1}
\end{aligned}\tag{46}$$

where we have used the abbreviations

$$\left[R_1\right]_{j-1/2}^{n-1}=-h_j\left[\begin{aligned}&\Pr(1-n)\left(v'\right)_{j-1/2}^{n-1}+nWe\left(vv'\right)_{j-1/2}^{n-1}+\left(2-\frac{(1-\xi)(1-m)}{4}-\frac{\alpha(1-\alpha)(1-m)}{4}\right)\left(f\,v\right)_{j-1/2}^{n-1}\\ &-\left(1-\frac{(1-\xi)(1-m)}{2}-\frac{\alpha(1-\alpha)(1-m)}{4}+Fs\xi\right)\left(u_{j-1}^{n-1}\right)^2+\Pr^2\xi^4\left(g_{j-1/2}^{n-1}\right)^2\\ &+\Pr(1-\xi)^4 s_{j-1/2}^{n-1}-\Pr\xi^2\left(M+Da^{-1}\right)u_{j-1/2}^{n-1}\end{aligned}\right]\tag{47}$$

$$\left[R_2\right]_{j-1/2}^{n-1}=-h_j\left[\begin{aligned}&\Pr(1-n)\left(p'\right)_{j-1/2}^{n-1}+\Pr nWe\xi^2\left(p\,p'\right)_{j-1/2}^{n-1}+\left(2-\frac{(1-\xi)(1-m)}{4}-\frac{\alpha(1-\alpha)(1-m)}{4}\right)\left(fp\right)_{j-1/2}^{n-1}\\ &-\left(2-\frac{\alpha(1-\alpha)(1-m)}{4}\right)\left(gu\right)_{j-1}^{n-1}-\Pr\xi^2\left(M+Da^{-1}\right)g_{j-1/2}^{n-1}-\Pr\xi^3 Fs\left(g_{j-1/2}^{n-1}\right)^2\end{aligned}\right]\tag{48}$$

$$[R_3]_{j-1/2}^{n-1} = -h_j \left[\begin{array}{l} (1+R)(t')_{j-1/2}^{n-1} + \left(2 - \frac{(1-\xi)(1-m)}{4} - \frac{\alpha(1-\alpha)(1-m)}{4}\right)(ft)_{j-1/2}^{n-1} \\ -\left(m - \frac{\alpha(1-\alpha)(1-m)}{4}\right)(us)_{j-1/2}^{n-1} \end{array} \right] \quad (49)$$

The boundary conditions are:

$$f_0^n = u_0^n = 0, g_0^n = s_0^n = 1, u_J^n = g_J^n = s_J^n = 0 \quad (50)$$

Stage 3: Quasilinearization of Non-Linear Keller Algebraic Equations

If we assume $f_j^{n-1}, u_j^{n-1}, v_j^{n-1}, g_j^{n-1}, p_j^{n-1} s_j^{n-1}, t_j^{n-1}$ to be known for $0 \le j \le J$, this leads to a system of *7J+7* equations for the solution of *7J+7* unknowns $f_j^n, u_j^n, v_j^n, g_j^n, p_j^n s_j^n, t_j^n$, $j = 0,1,2,...,J$. This non-linear system of algebraic equations is linearized by means of Newton's method.

Stage 4: Block-tridiagonal Elimination Solution of Linear Keller Algebraic Equations

The linearized system is solved by the block-elimination method, since it possesses a block-tridiagonal structure. The bock-tridiagonal structure generated consists of *block matrices*. The complete linearized system is formulated as a *block matrix system,* where each element in the coefficient matrix is a matrix itself, and this system is solved using the efficient Keller-box method. The numerical results are strongly influenced by the number of mesh points in both directions. After some trials in the η-direction (radial coordinate) a larger number of mesh points are selected whereas in the ξ-direction (tangential coordinate) significantly less mesh points are utilized. $\eta_{\max}$ has been set at 25 and this defines an adequately large value at which the prescribed boundary conditions are satisfied. ξ_{max} is set at 3.0 for this flow domain. Mesh independence is achieved in the present computations. The numerical algorithm is executed in **MATLAB** on a PC. The method demonstrates excellent stability, convergence and consistency, as elaborated by Keller [54].

This code has previously resolved many challenging multi-physical fluid dynamics problems including enrobing viscoplastic boundary layer coating flow with hydrodynamic slip [57], magnetic viscoelastic nanofluid coating of a cylinder [58], radiative heat transfer in hydromagnetic non-Newtonian third grade coating of a cone [59], mixed convection Falkner-Skan nanofluid dynamics [60], pseudoplastic thermal coating of a cone [61], inclined substrate coating flow with magnetic field, radiation, viscous heating and entropy generation effects [62] and magnetic nanofluid fuel cell internal convection flows with Ohmic dissipation [63, 64]. The Keller-Box discretization is fully coupled at each step which reflects the physics of parabolic systems – which are also fully coupled. Discrete calculus associated with the Keller-Box scheme has also been shown to be fundamentally different from all other physics capturing numerical methods. The Keller Box Scheme comprises four stages which are summarized in **Fig. 2**. LU decomposition is utilized in the 4th and final stage [58-64]. A typical Keller box (cell) and boundary layer grid design is given in **Fig. 3**. The 9th order coupled system defined by Eqns. (17)-(19) is reduced to 7 first order differential equations via suitable variable substitutions. The code is executed in several minutes on a laptop or desktop PC and excellent convergence is achieved. To validate the Keller box code, verification is conducted against the special cases considered earlier in Anil Kumar and Roy [65] and Sparrow and Cess [66] in the absence of tangent hyperbolic parameters i. e. $n = 0$, *$We = 0$, for isothermal behaviour ($m = 0$) and neglecting porous medium effects i. e. $Da \to \infty$, $Fs = 0$, for the steady state case, over a range of Prandtl numbers (Pr). Both magnetic ($M = 0$) and non-magnetic cases ($M = 1$) are however considered in the validations.*

Table 1: Comparison values of $-\theta'(\xi, 0)$ for various values of Pr and M

Pr	Present Keller Box Results		Kumar and Roy [65]		Sparrow and Chess [66]	
	$M = 0$	$M = 1$	$M = 0$	$M = 1$	$M = 0$	$M = 1$
0.5	0.0425	0.2818	0.0426	0.2819	0.0428	0.2820
1.0	0.0274	0.1936	0.0282	0.1939	0.0244	0.1940
2.0	0.0105	0.0980	0.0107	0.0981	0.0108	0.0982
3.0	0.0059	0.0586	0.0061	0.0587	0.0061	0.0588
4.0	0.0040	0.0398	0.0041	0.0344	0.0041	0.0395

Table 1 documents the Nusselt number, $Nu = -\theta'(\xi, 0)$ at the cone surface and very close correlation is achieved between the Keller box results and previous studies. Confidence in the accuracy of the Keller box solutions executed in MATLAB is therefore established.

4. GRAPHICAL AND TABULAR RESULTS AND DISCUSSION

The Keller box computations are visualized in **Figs. 4- 9 a, b, c** for the effects of selected control parameters on radial, tangential velocity and temperature with spanwise (transverse) coordinate). In these graphs, the location $\xi = 1$ is considered along the cone surface (wall). Aqueous-based magnetic polymers are considered. All data is obtained to represent physically realistic scenarios [47-51]. **Table 2** provides solutions for the primary shear stress (C_{fx}), secondary shear stress (C_{gx}) and Nusselt number (Nux) with variation in stream-wise coordinate and all key parameters. All data utilized is given in the figure captions and corresponds to highly porous media (*Da* =2) and weak magnetic field (*M* = 0.5) with weak second order inertial (Forchheimer) drag (*Fs* = 0.5). **Figures 4a-c** depicts the effects of Weissenberg number (*We*) on the axial velocity (f'), tangential velocity (g) and temperature (θ) distributions through the boundary layer regime. **Fig 4a** reveals that with increment in *We*, axial velocity is strongly damped in the vicinity of the cone surface (η=0); at further distances into the boundary layer no tangible modification is computed. The Weissenberg number We is required to simulate the nonlinear relation between shear stress and strain rate in the non-Newtonian nanofluid. It characterizes the ratio of *elastic to viscous forces* in the magnetic polymer. It also expresses the ratio of *fluid relaxation time to specific time*.

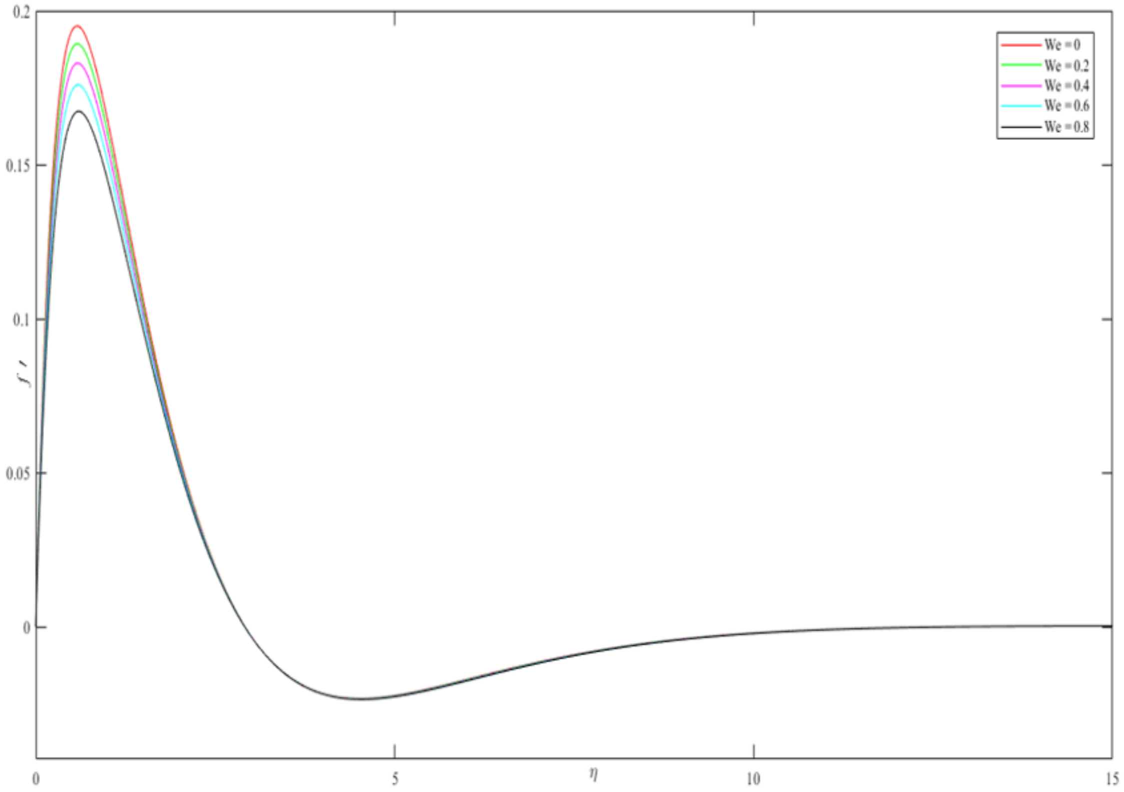

Fig. 4a) Effect of *Weissenberg number, We* on axial velocity with ξ *=1, Pr = Da =2, n=0.3, m = 1, M =R = Fs = 0.5.*

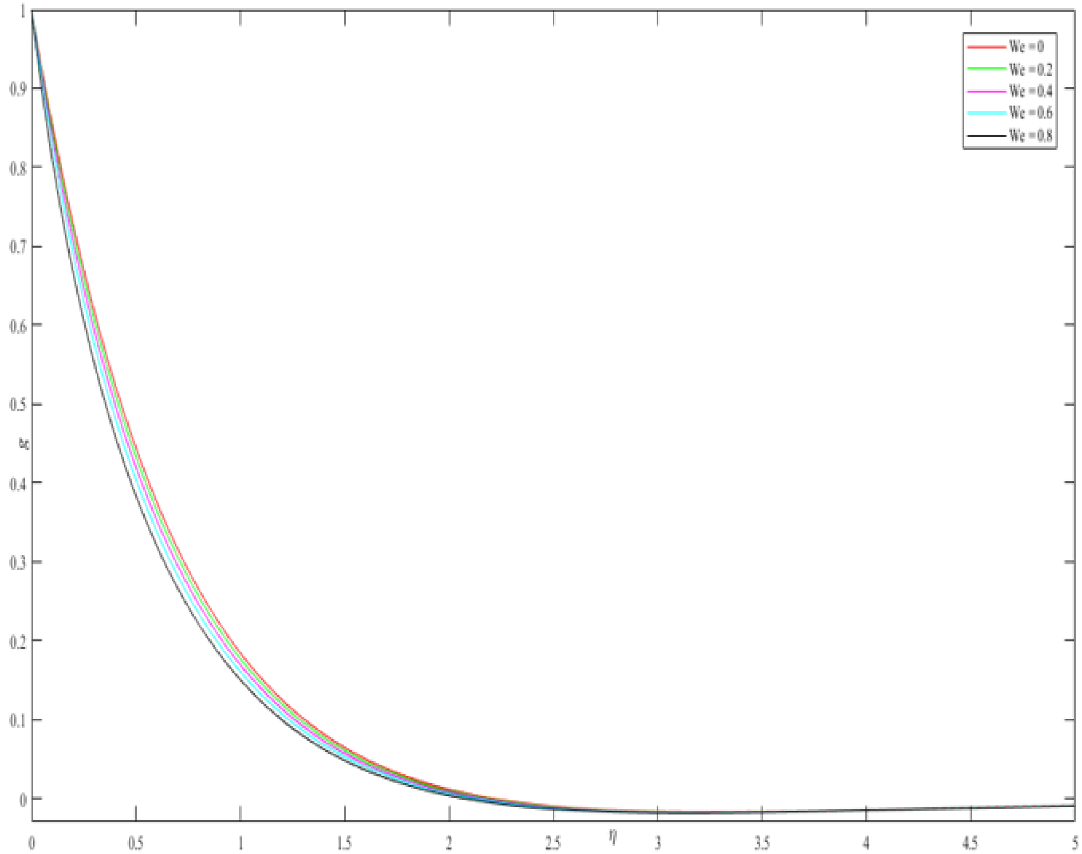

Fig. 4b) *Weissenberg number, We,* effect on tangential velocity with ξ *=1, Pr=Da =2, n=0.3, m = 1, We = 0.3, M =R = Fs =0.5.*

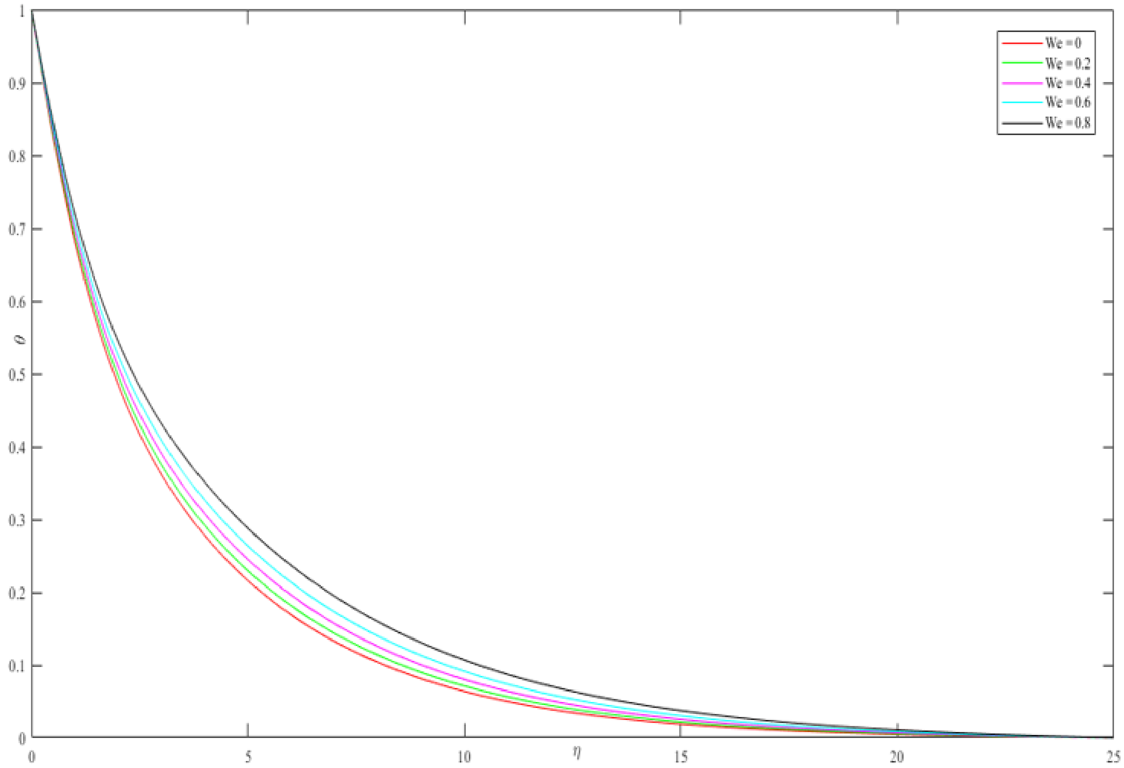

Fig. 4c) *Weissenberg number, We,* effect on temperature with ξ *=1, Pr = Da = 2, n=0.3, m = 1, M =R = Fs =0.5.*

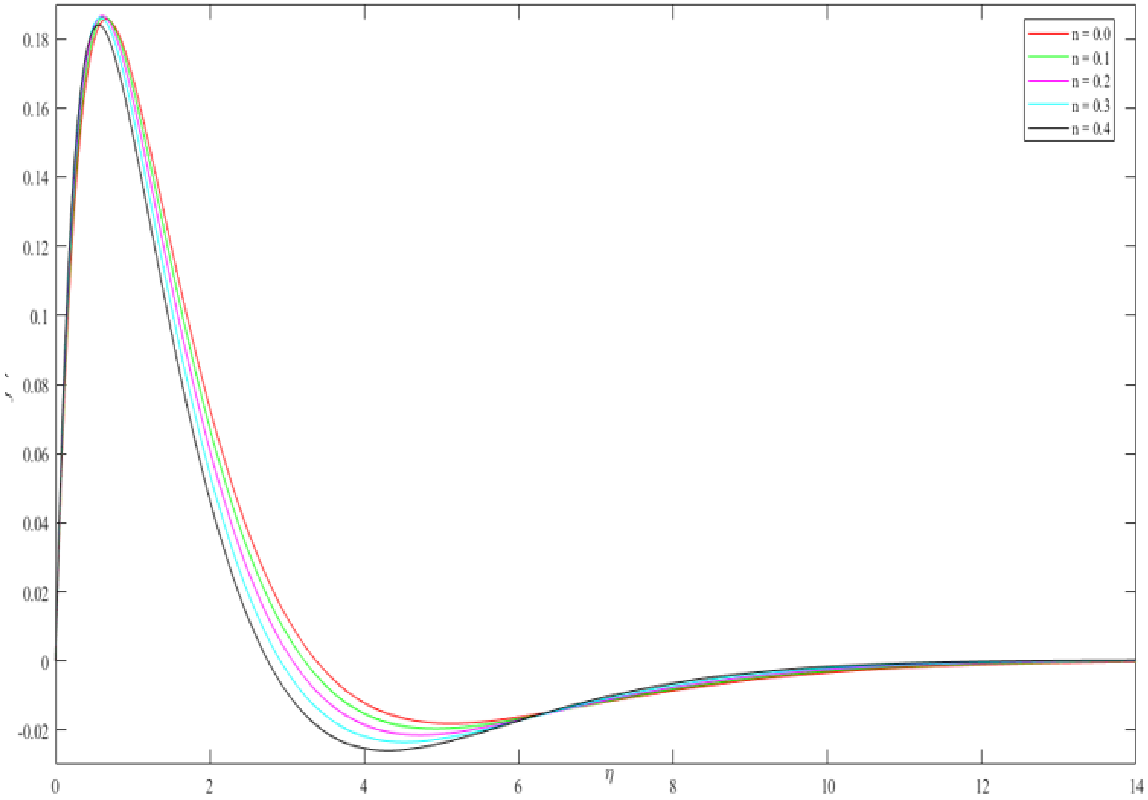

Fig. 5a) *Tangent hyperbolic power law index, n,* effect on axial velocity with $\xi = 1$, $Pr = Da = 2$, $m = 1$, $We = 0.3$, $M = R = Fs = 0.5$.

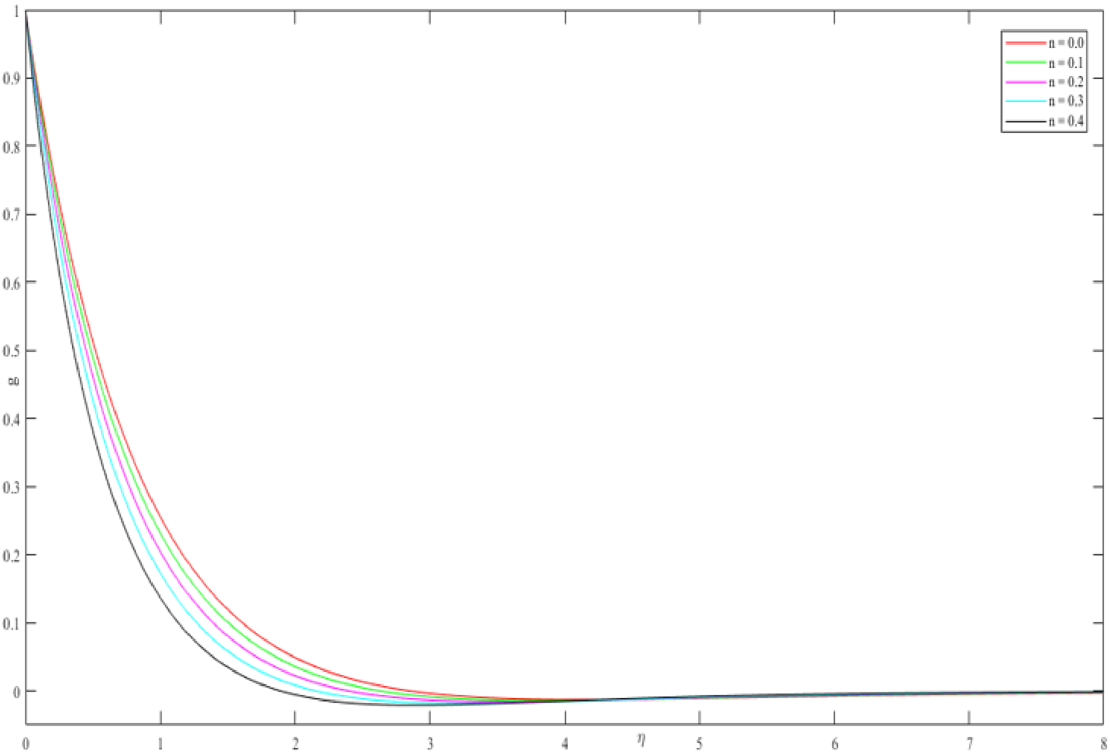

Fig. 5b) *Tangent hyperbolic power law index, n,* effect on tangential velocity; $\xi = 1$, $Pr = Da = 2$, $m = 1$, $We = 0.3$, $M = R = Fs = 0.5$.

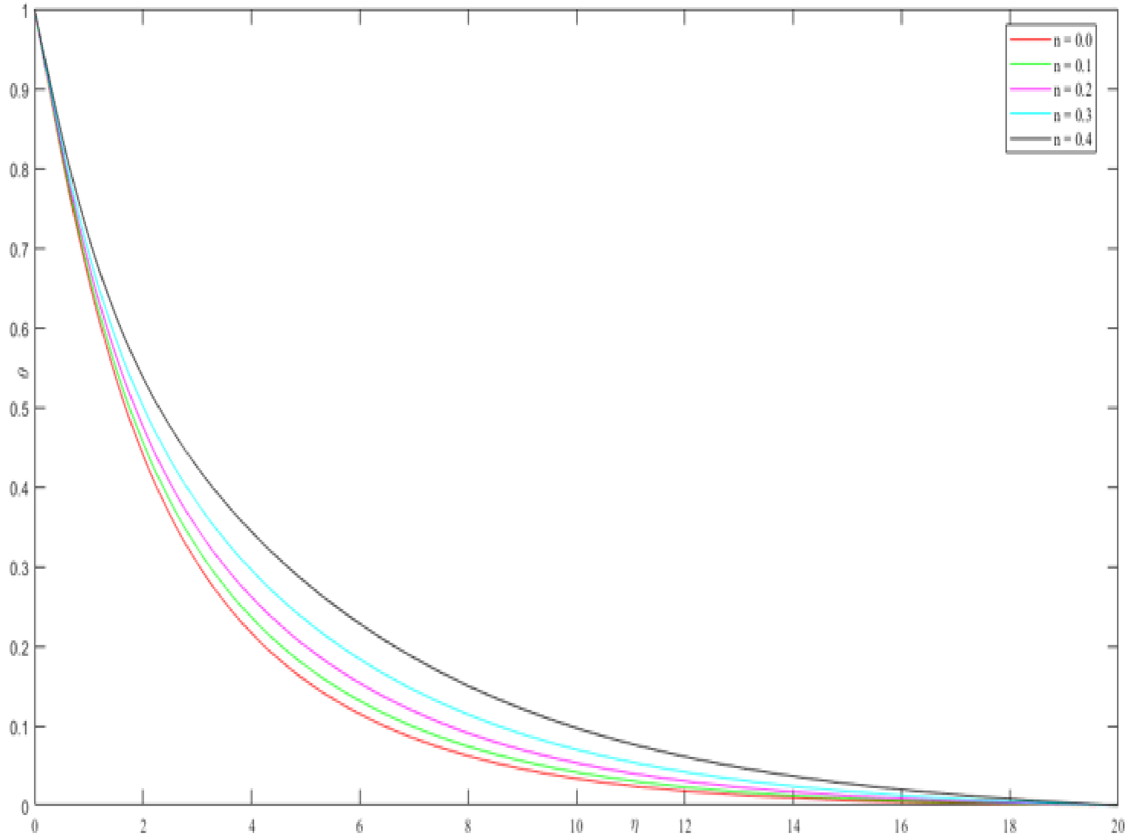

Fig. 5c) *Tangent hyperbolic power law index, n,* effect on temperature;*ξ =1, Pr =Da=2, m = 1, We=0.3, M =R = Fs =0.5.*

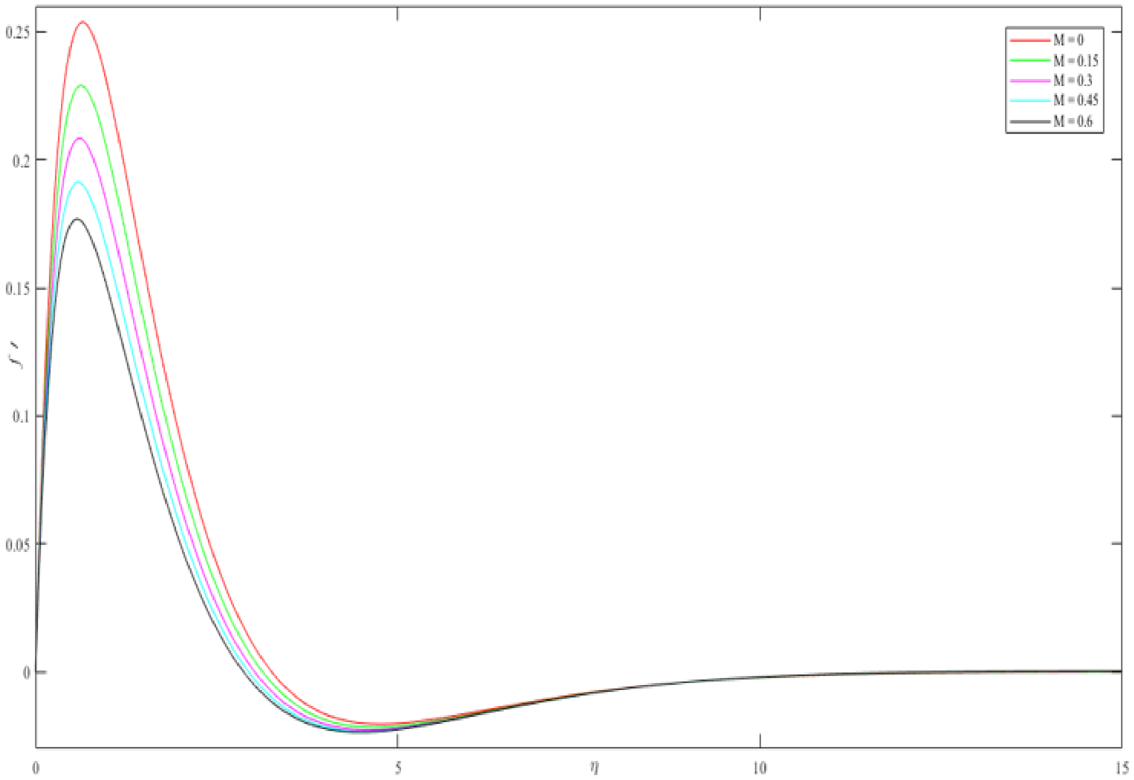

Fig. 6a) *Magnetic interaction parameter, M,* effect on axial velocity;*ξ =1, Pr =Da=2, m = 1, n=We=0.3, R = Fs =0.5.*

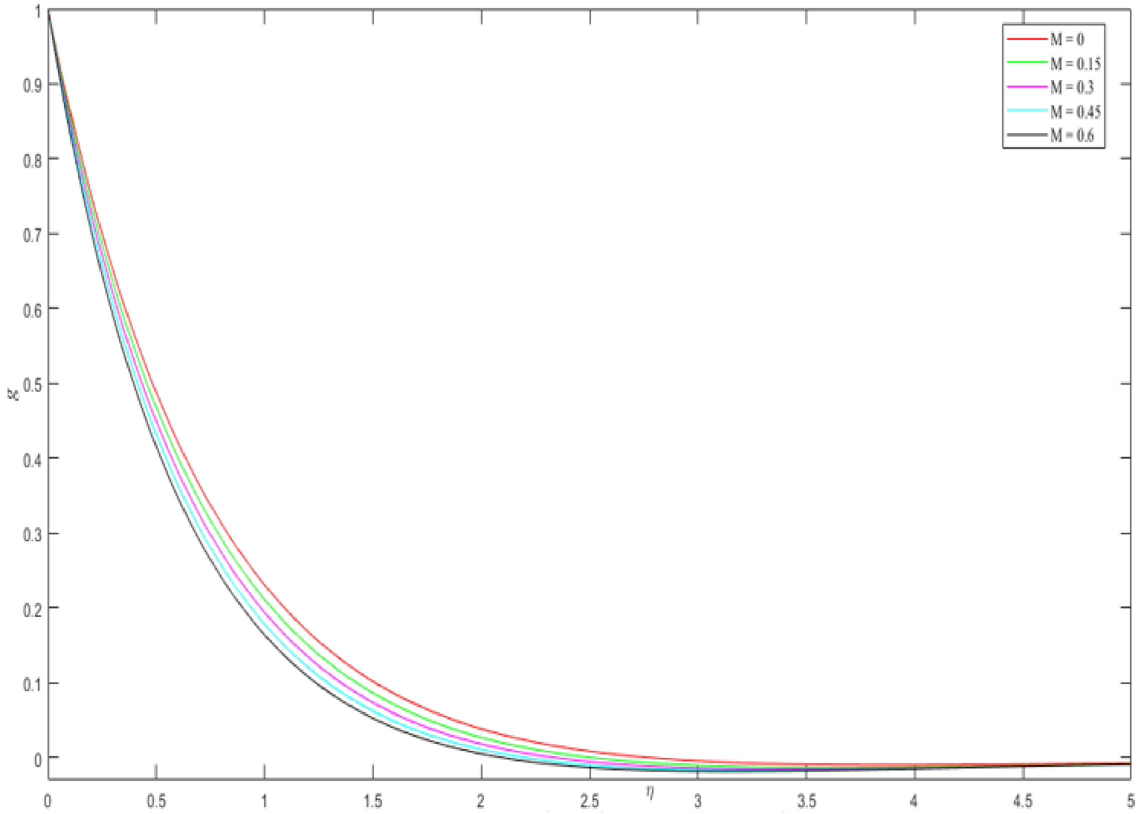

Fig. 6b) *Magnetic interaction parameter, M,* effect on tangential velocity;*ξ =1, Pr =Da=2, m = 1, n=We=0.3, R = Fs =0.5.*

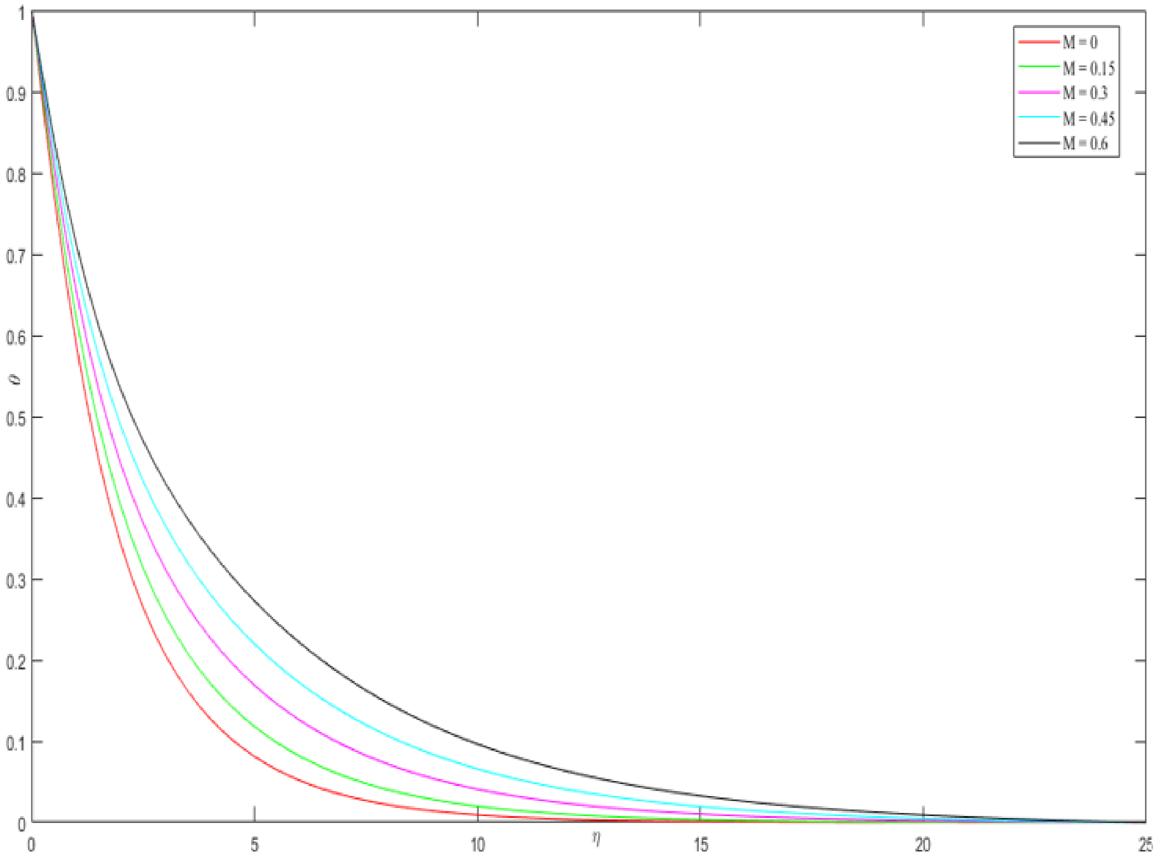

Fig. 6c) *Magnetic interaction parameter, M,* effect on temperature;*ξ =1, Pr =Da=2, m = 1, n=We=0.3, R = Fs =0.5.*

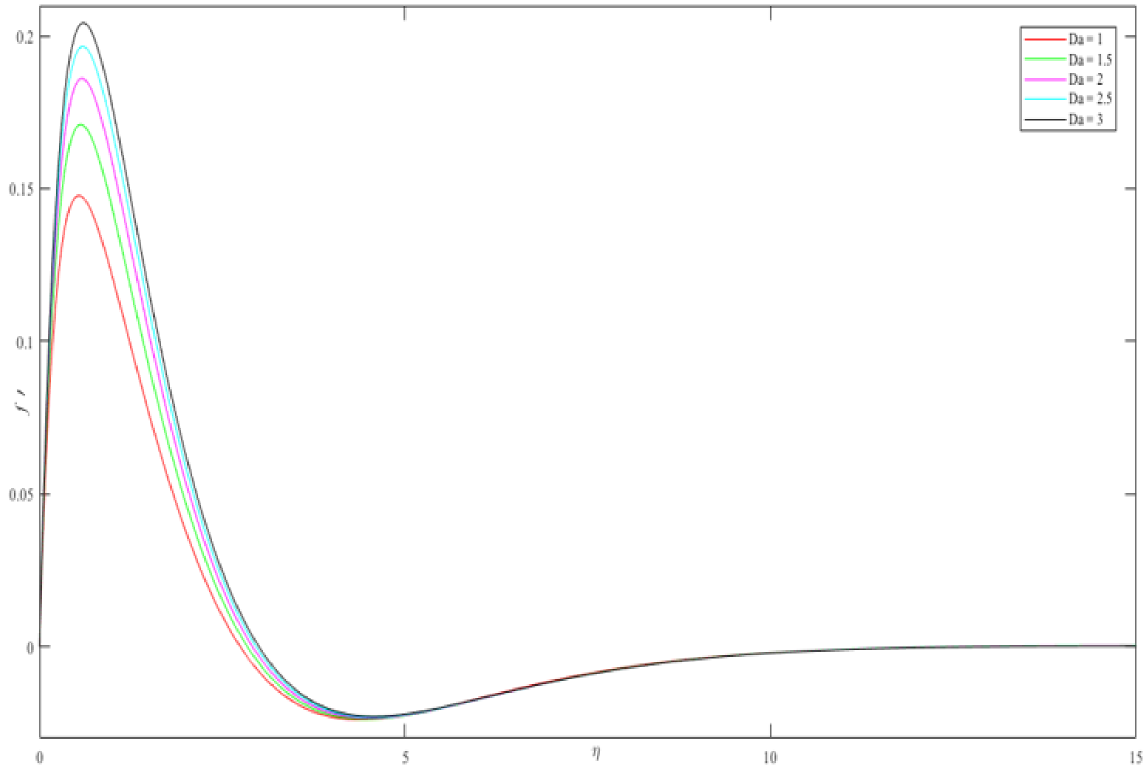

Fig. 7a) *Darcy parameter, Da,* effect on axial velocity;*ξ =1, Pr =2, m = 1, n=We=0.3, M=R = Fs =0.5.*

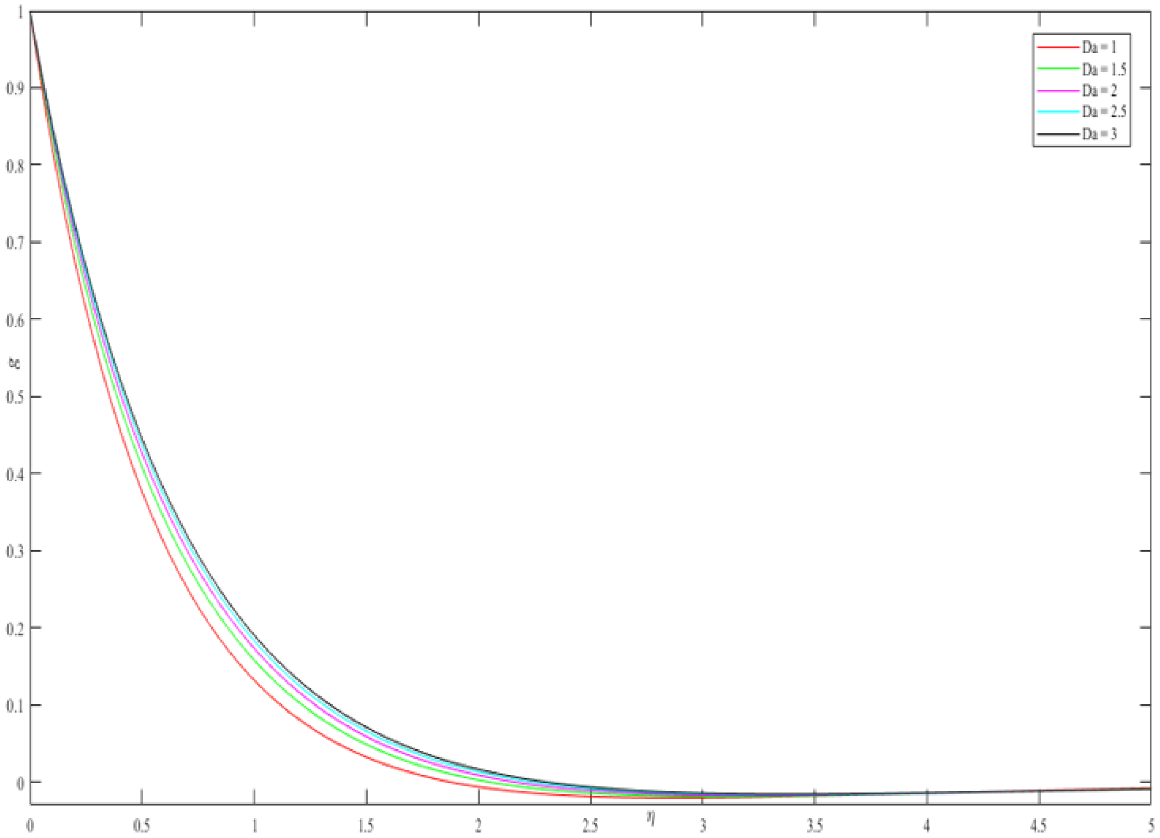

Fig. 7b) *Darcy parameter, Da,* effect on tangential velocity;*ξ =1, Pr =2, m = 1, n=We=0.3, M=R = Fs =0.5.*

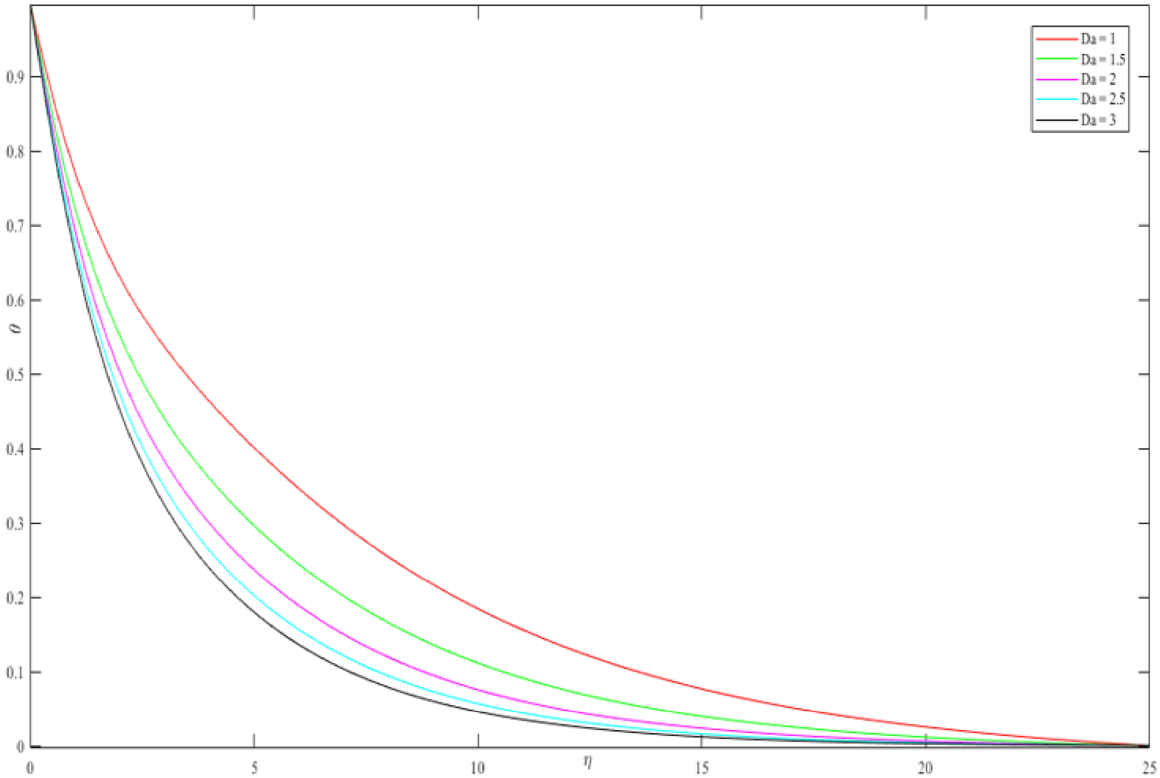

Fig. 7c) *Darcy parameter*, *Da*, effect on temperature;*ξ =1*, *Pr =2*, *m = 1*, *n=We=0.3*, *M=R = Fs =0.5.*

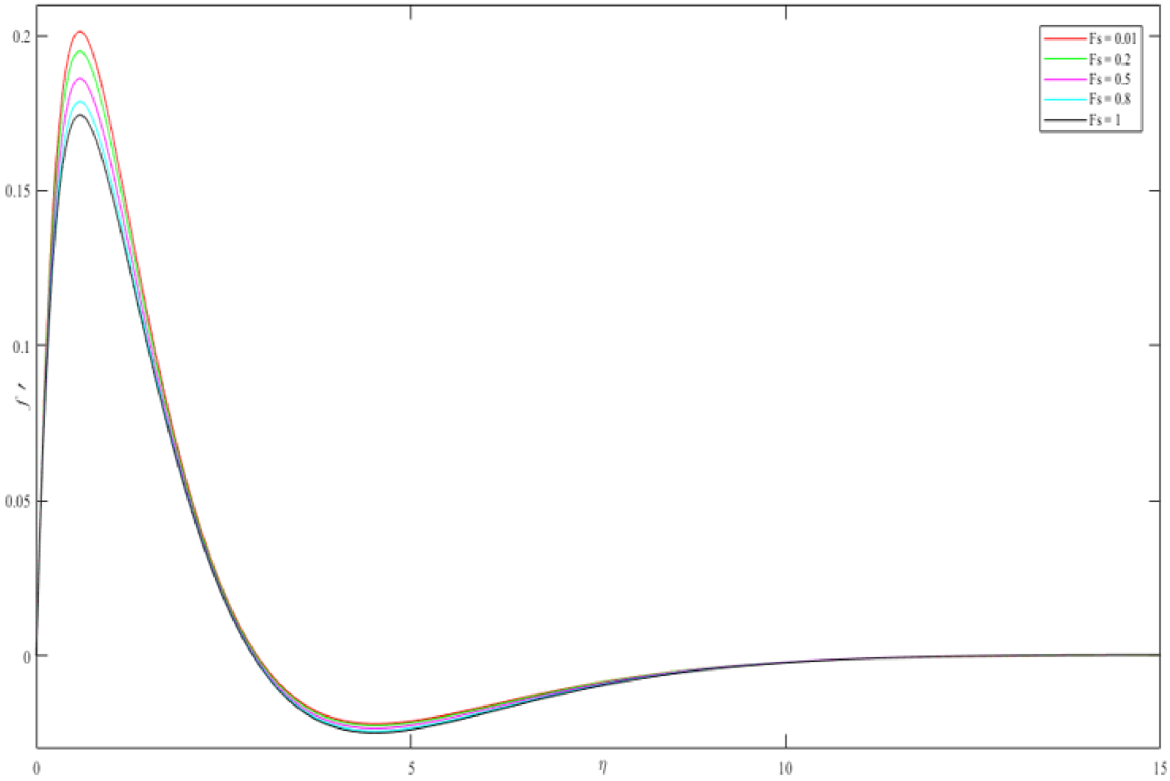

Fig. 8a) *Forchheimer parameter*, *Fs*, effect on axial velocity;*ξ =1*, *Pr =2*, *m = 1*, *n=We=0.3*, *M=R = Da =0.5.*

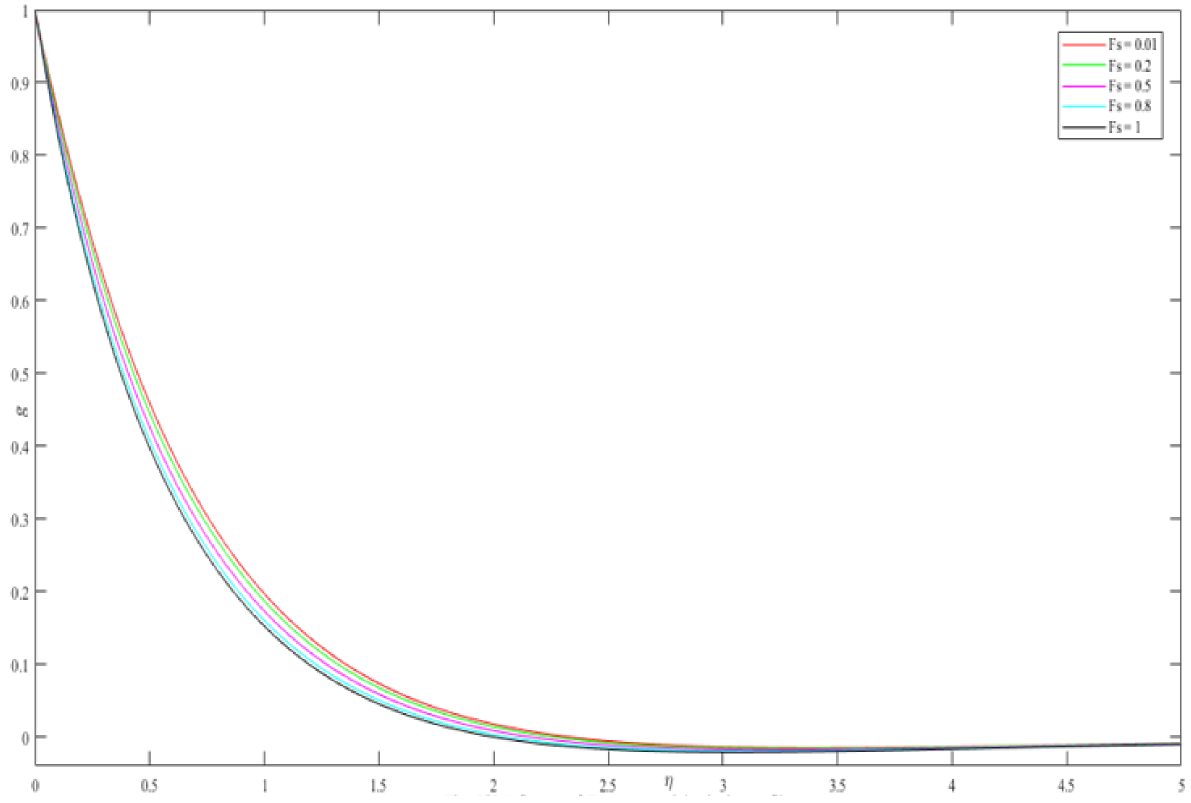

Fig. 8b) *Forchheimer parameter, Fs,* effect on tangential velocity;*ξ =1, Pr =2, m = 1, n=We=0.3, M=R = Da =0.5.*

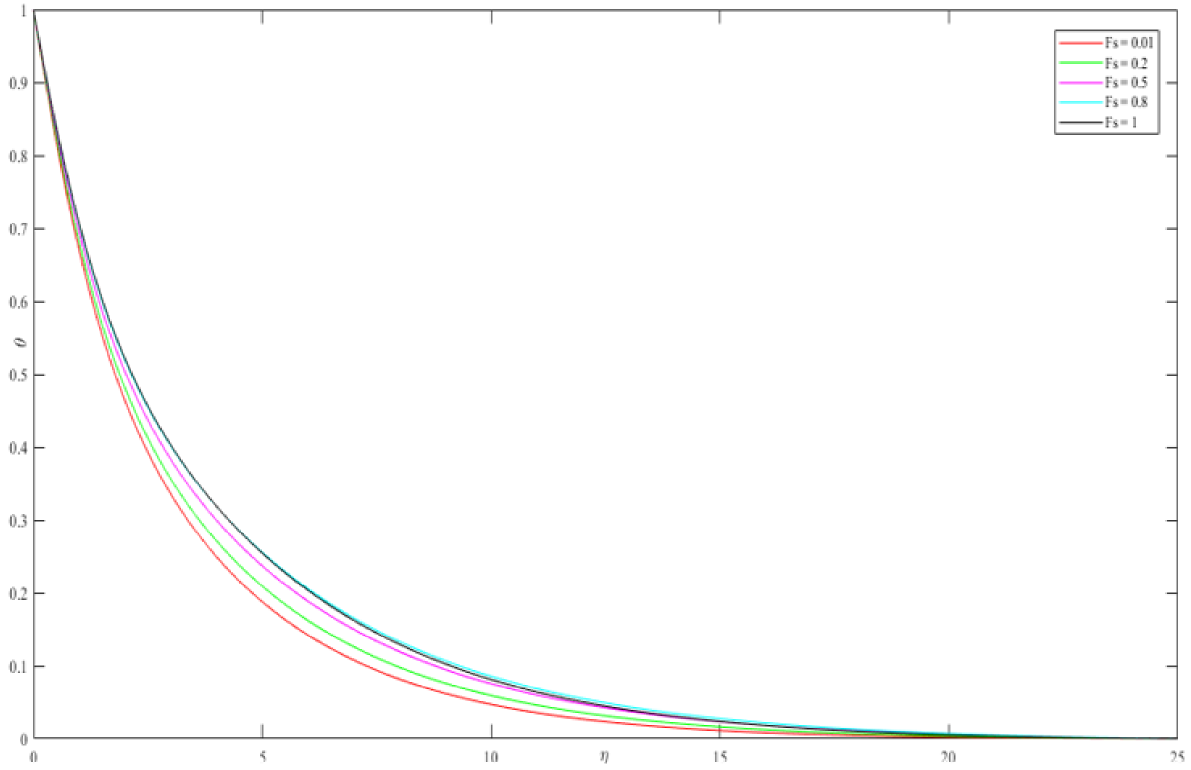

Fig. 8c) *Forchheimer parameter, Fs,* effect on temperature;*ξ =1, Pr =2, m = 1, n=We=0.3, M=R = Da =0.5.*

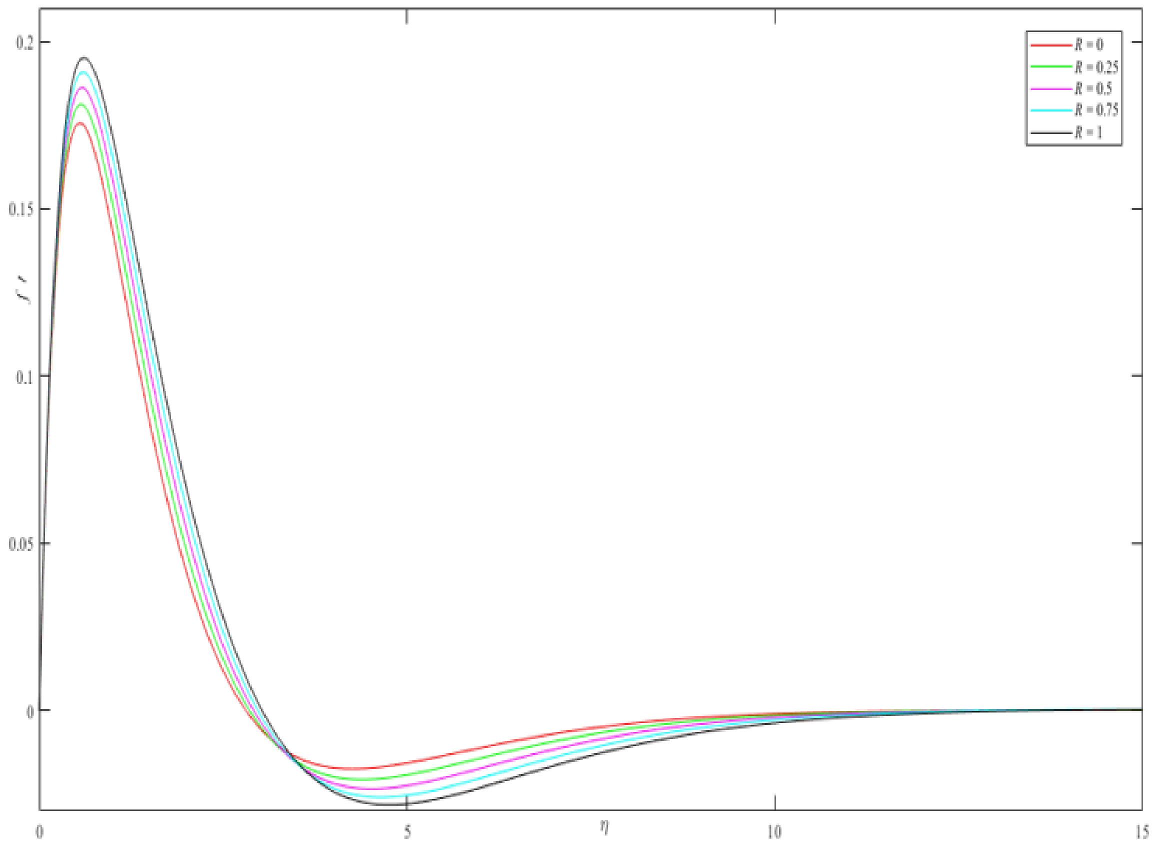

Fig. 9a) *Rosseland radiative parameter, R,* effect on axial velocity;*ξ =1, Pr =Da=2, m = 1, n=We=0.3, M=Fs =0.5.*

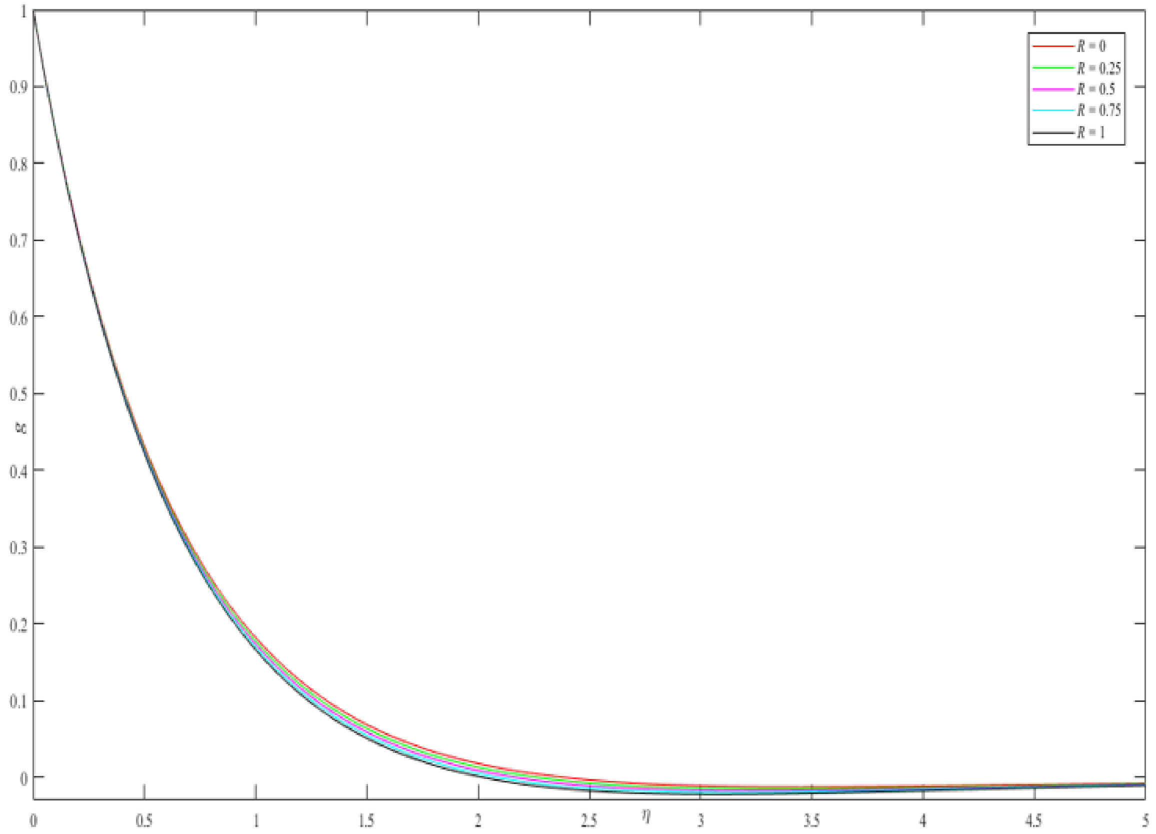

Fig. 9b) *Rosseland radiative parameter, R,* effect on tangential velocity;*ξ =1, Pr =Da=2, m = 1, n=We=0.3, M=Fs =0.5.*

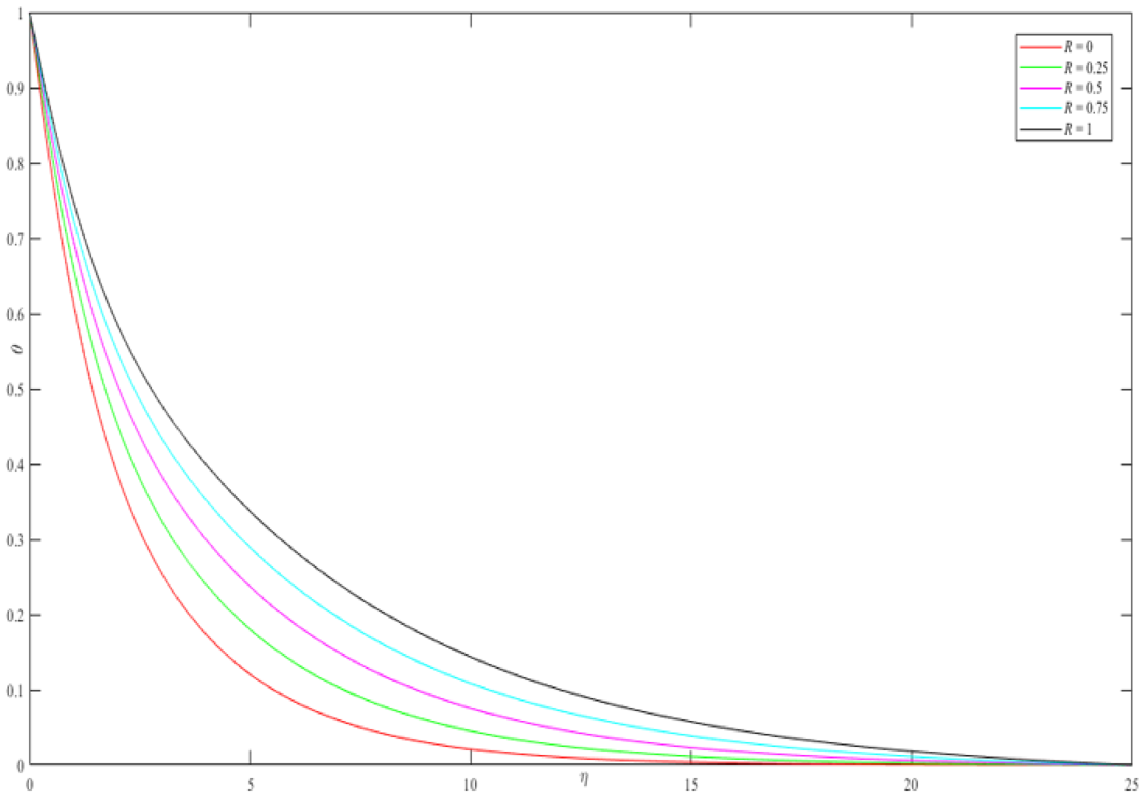

Fig. 9c) *Rosseland radiative parameter, R,* effect on temperature; $\xi=1$, $Pr=Da=2$, $m=1$, $n=We=0.3$, $M=Fs=0.5$.

Table 2: Values of C_{fx}, C_{gx} and Nu for different of n, We, M, Da, Fs, R, Pr, m and ξ .

n	We	M	Da	Fs	R	Pr	m	$\xi = 0$			$\xi = 1.0$		
								C_{fx}	C_{gx}	Nu	C_{fx}	C_{gx}	Nu
0								0.7696	0	0.8847	0.7933	-2.6356	0.5758
0.1								0.7454	0	0.9007	0.7528	-2.4850	0.5646
0.2								0.7195	0	0.9184	0.7088	-2.3207	0.5496
0.3								0.6915	0	0.9381	0.6600	-2.1375	0.5290
0.4								0.661	0	0.9602	0.6032	-1.9255	0.4989
	0							0.6863	0	0.9415	0.6769	-2.2198	0.5499
	0.2							0.6898	0	0.9392	0.6660	-2.1660	0.5363
	0.4							0.6931	0	0.9370	0.6533	-2.1076	0.5214
	0.6							0.6963	0	0.9349	0.6369	-2.0423	0.5042
	0.8							0.6995	0	0.9328	0.6129	-1.9619	0.4831
		0						0.6915	0	0.9381	0.7830	-1.8093	0.7064
		0.15						0.6915	0	0.9381	0.7399	-1.9123	0.6501
		0.3						0.6915	0	0.9381	0.7025	-2.0112	0.5942
		0.45						0.6915	0	0.9381	0.6700	-2.1065	0.5445
		0.6						0.6915	0	0.9381	0.6414	-2.1984	0.4993

			1					0.6915	0	0.9381	0.5803	-2.1284	0.4046
			1.5					0.6915	0	0.9381	0.6299	-2.2382	0.4807
			2					0.6915	0	0.9381	0.6600	-2.1375	0.5890
			2.5					0.6915	0	0.9381	0.6803	-2.0751	0.5606
			3					0.6915	0	0.9381	0.6949	-2.0327	0.5828
				0.01				0.6915	0	0.9381	0.6970	-1.8963	0.5710
				0.2				0.6915	0	0.9381	0.6816	-1.9931	0.5528
				0.5				0.6915	0	0.9381	0.6600	-2.1375	0.5290
				0.8				0.6915	0	0.9381	0.6411	-2.2729	0.5118
				1				0.6915	0	0.9381	0.6298	-2.3589	0.5051
					0			0.6425	0	0.7134	0.6456	-2.1237	0.4553
					0.25			0.6693	0	0.8299	0.6532	-2.1310	0.4956
					0.5			0.6915	0	0.9381	0.6600	-2.1375	0.5290
					0.75			0.7104	0	1.0396	0.6661	-2.1435	0.5579
					1			0.7269	0	1.1357	0.6717	-2.1490	0.5840
						0.5		0.6207	0	0.8070	0.2700	-0.5863	0.2463
						1		0.6575	0	0.8778	0.3954	-1.1012	0.3542
						2		0.6915	0	0.9381	0.6600	-2.1375	0.5290
						3		0.7098	0	0.9678	0.9283	-3.1747	0.6756
						9		0.7493	0	1.0234	2.8467	-9.5502	1.2444
						10		0.7455	0	1.0197	2.5561	-10.5178	1.3855
							1	0.6915	0	0.9381	0.6600	-2.1375	0.5290
							1.2	0.6784	0	0.9667	0.6124	-2.1949	0.5448
							1.5	0.6608	0	1.0060	0.5912	-2.1640	0.5916
							2	0.6357	0	1.0636	0.5701	-2.1391	0.6093
							3	0.5964	0	1.1585	0.5503	-2.1199	0.6911

For large values of *We*, fluid relaxation time will greatly exceed the time scale of the flow and elastic stresses will be dominant. The reverse behavior will arise when relaxation time is exceeded by time scale of the flow for which the viscous effects will dominate, and elastic effects will subside. The magnetic polymer is therefore able to move with less tensile stress impedance when *We* is reduced, and this produces the observed acceleration in axial flow at lower Weissenberg numbers. Similarly, a very strong reduction in tangential velocity is computed in Fig 4b with increasing Weissenberg number. However, temperature (Fig. 4c) is substantially elevated with increment in Weissenberg number and there is an associated increase in thermal boundary layer thickness. It is interesting to note that We arises only in the modified shear terms, $+nW_ef''f'''$ in the axial momentum eqn. (17) and $+Pr\,n\,W_e\xi^2 g'g''$ in the tangential momentum eqn. (18), but is absent in the energy conservation eqn. (19). However, via strong coupling between the axial momentum (17) and energy eqn. (19), for example via the term, $+Pr(1-\xi)^4\,\theta$ in the former and numerous terms in the latter, viz, $+\left(2-\frac{(1-\xi)(1-m)}{4}\right)f\theta', -mf'\theta, \xi(1-\xi)\left(\frac{1-m}{4}\right)\left(f'\frac{\partial\theta}{\partial\xi}-\theta'\frac{\partial f}{\partial\xi}\right)$ the Weissenberg number exerts a strong indirect influence on temperature field.

Figs 5a-c depict the response in axial velocity (f'), tangential velocity (g) and temperature (θ) distributions with a variation in tangent hyperbolic index (n). This parameter arises in the modified shear term, $Pr(1-n)f'''$ in the axial momentum eqn. (17). For the case of $n = 0$ the tangent hyperbolic effect is negated and the model contracts to the *Newtonian viscous fluid*. As n is increased the pseudoplasticity (shear-thinning) of the magnetic polymer is increased and viscosity is modified. This causes an initial very weak increase in axial velocity magnitudes closer to the cone surface. However, very quickly the axial velocity is damped implying that axial flow deceleration is generally produced further from the cone surface (wall) with greater values of n. Further towards the free stream, the initial accelerating effect is resumed indicating that rheological shear-thinning behaviour has a complex influence on axial velocity distribution. The response changes with location from the cone surface (wall), as seen in Fig. 5a. Entanglement of the magnetic polymer chains is also associated with stronger pseudoplastic behaviour, and this may also contribute to the modification in viscosity and the variable response in axial velocity distributions. Fig 5b demonstrates that a strong reduction is computed in tangential velocity with increasing n values. A weak tangential back flow (flow reversal) is computed at intermediate distances from the cone surface. The coating boundary layer thickness maybe adjusted via the deployment of different shear-thinning polymers. Both axial and tangential velocity distributions exhibit generally very smooth decays into the free stream confirming that a sufficiently large infinity boundary condition has been utilized in the Keller box computations. Fig. 5c shows that temperature is strongly enhanced with elevation in rheological power-law index, n values. Asymptotically smooth decays are computed from the cone surface to the free stream (edge of the boundary layer). Thermal boundary layer thickness is also decreased with greater pseudoplasticity (higher n values) of the magnetic polymer. Although the parameter, n, does not arise in the energy eqn. (19), nevertheless, indirectly thermal diffusion is impacted by the coupling with the axial velocity field, via the terms, $\left(2-\frac{(1-\xi)(1-m)}{4}\right)f\theta', -mf'\theta, \xi(1-\xi)\left(\frac{1-m}{4}\right)\left(f'\frac{\partial\theta}{\partial\xi}-\theta'\frac{\partial f}{\partial\xi}\right)$. When tangent hyperbolic index (n) becomes zero, the shear-thinning effect vanishes, and minimal temperature is observed.

Figures 6a-c visualize the impact of magnetic interaction parameter M, on the axial velocity) (f'), tangential velocity (g) and temperature (θ) distributions with transverse coordinate (η). The parameter $M = \dfrac{\sigma B_0^2}{\rho \Omega \sin\varphi}$ defines the ratio of Lorentzian electromagnetic force and the rotational inertial (centrifugal) force in the regime. It arises in the axial momentum eqn. (17) and is also present in the tangential eqn. (18), respectively in the terms, $-Pr\xi^2 M\, f^{/}$ and $-Pr\xi^2 M$ g. These terms are the Lorentzian body force components in the axial and tangential (circumferential) directions. For M = 0 magnetic field effects vanish, and the polymer becomes electrically non-conducting. **Fig. 6a** reveals that shows that stronger magnetic field strongly damps the axial flow, in particular in the vicinity of the cone surface. Peak velocities are also progressively displaced further from the cone surface with increment in M. Maximum axial velocity clearly arises for the non-magnetic case (M = 0) and this will produce a thicker momentum boundary layer. All axial velocity profiles converge in the free stream. In other words, after a critical distance from the cone surface into the boundary layer the magnetic field effect is negated. The key modification in momentum characteristics is therefore achieved in proximity to the cone surface. **Fig. 6b** shows that there is a significant damping in tangential flow with larger values of M. However distinct from the axial velocity topologies, there is no near-wall peak computed. A consistent decay in tangential velocities is computed throughout the entire boundary layer regime from the cone surface to the free stream Peak tangential velocity always arises at the cone surface (wall). Again, maximum tangential flow acceleration is produced with the elimination of the Lorentzian magnetic retarding force for M = 0. A slight tangential flow reversal (negative velocities) is computed at large distance from the cone surface. In the free stream tangential velocity vanishes in accordance with the infinity boundary condition prescribed in eqn. (20). **Fig. 6c** indicates that temperature is substantially boosted with elevation in magnetic interaction parameter, M. Asymptotic decays are computed in all cases. The excess work expended in dragging the magnetic polymer against the action of the radial magnetic field manifests in heat dissipation. This heats the magnetic polymer and elevates thermal boundary layer thickness. The effect is sustained at all locations from the cone surface to the free stream. Clearly minimum temperature and thermal boundary layer thickness correspond to the non-magnetic case (M = 0).

Figures 7a-c illustrate the effect of the Darcy number, Da, on the axial velocity $\left(f'\right)$, tangential velocity (g) and temperature (θ) distributions with transverse coordinate (η). This parameter features in both momentum balance eqns. (17) and (18) in the terms, $-Pr\xi^2(\frac{1}{Da})f^{\,/}$ and

$-Pr\xi^2\left(\frac{1}{Da}\right)g$. These are the Darcian axial and tangential body force components and are linear terms. $Da = \frac{K\Omega\, sin\,\varphi}{\nu s}$ and when Da tends to infinity, the porous medium has infinite permeability for which both Darcian body forces vanish. Fig 7a clearly shows that with increment in *Da*, the axial velocity is strongly accentuated, and this effect is maximized near the cone surface. Clearly larger permeability implies a reduction in solid fibers which are present to impede the axial flow and this diminishes the Darcian resistance which results in axial flow acceleration. Peak velocity is pushed further from the wall (cone surface) with increasing Darcy parameter. The topologies are similar to those computed with magnetic interaction parameter earlier. Fig 7b shows that strong accentuation in tangential velocity also accompanies an increment in Darcy parameter. A consistent response is computed throughout the boundary layer regime. Again, evidently percolation of the magnetic polymer through the porous medium is assisted with greater permeability and the associated reduction in Darcian bulk matrix impedance to the tangential flow. Clearly the deployment of a porous medium offers an excellent Fig. 7c demonstrates that a strong damping in temperature is produced by increasing Darcy parameter. The depletion in solid fibers in the porous matrix associated with higher permeability manifests in a suppression in thermal conduction. This curtails heat diffusion in the regime and cools it. Thermal boundary layer thickness on the rotating cone surface is therefore decreased. Lower permeability porous media clearly achieve much higher temperatures than higher permeability media.

Figures 8a-c illustrate the effect of the Forchheimer number, *Fs*, on the axial velocity $\left(f\,'\right)$, tangential velocity (g) and temperature (θ) distributions with transverse coordinate (η). $Fs = \Lambda\chi\sqrt{\frac{\nu}{\Omega\sin\varphi}}$ and simulates the impact of nonlinear (second order) porous media drag. As with Darcy number, it features in both axial and tangential Forchheimer drag components, for example $-Fs\,(f')^2$ in eqn. (17). It is clearly quadratic whereas Darcian drag components are linear. For the case of Darcy-Brinkman flow, Fs = 0 and inertial drag effects vanish. Fig 8a shows that a marked depletion in axal velocity is induced with increment in Forchheimer number since stronger inertial impedance is present which opposes axial flow. The effect is optimized near the cone surface and further away a weaker deceleration is computed in axial flow with greater Forchheimer number. In the free stream no tangible influence of Forchheimer number is observed on axial flow. Fig 8b shows that a sustained deceleration in tangential flow is induced with greater Forchheimer number. There is no secondary dip in profiles as with the axial flow. Peak velocity corresponds to the weak Forchheimer scenario (*Fs*=0.01) at all location’s transverse to the cone surface into the free stream. Fig 8c reveals that larger Forchheimer number produces a substantial heating effect in the regime. Temperatures are consistently elevated at all values of transverse coordinate (η). Thermal boundary layer thickness is therefore minimal for the weak Forchheimer drag case ($Fs = 0$) and maximum for the strong Forchheimer case ($Fs = 1$). Of course, our simulations are limited to isotropic and non-tortuous porous media. However, the significant influence of linear Darcian impedance and second order inertial porous drag on manipulating flow and thermal characteristics in rotational coating applications is clearly demonstrated.

Figures 9 a-c illustrate the effect of the Rosseland-Boltzmann radiative parameter (also known as Stark number) on axial velocity $\left(f'\right)$, tangential velocity (g) and temperature (θ) distributions with transverse coordinate (η). $R = \frac{16\sigma^* T_\infty^3}{3k\,k^*}$ and represents the relative role of radiative heat transfer to conduction heat transfer in the regime. This parameter only features in the augmented thermal diffusion term, $\theta''(1+R)$, in eqn. (19). Fig 9a demonstrates that an increment in R i. e. stronger radiative flux initially boosts the axial velocity noticeably in close proximity to the rotating cone surface. The near-wall peak is progressively displaced further from the wall with larger R values. Clearly an increment in radiative heat flux energizes the boundary layer and influences the axial and tangential flow via coupling with many terms in both eqns. (17) and (18) with eqn. (19). However further from the wall, at intermediate distances into the boundary layer, there is a dampening in axial flow. Towards the free stream this deceleration with stronger radiative flux is eliminated. Near the cone surface the non-radiative case ($R = 0$) produces minimal axial velocity whereas further from the cone surface it achieves maximum magnitudes, although these magnitudes are much smaller than those computed near the cone surface. Fig 9b shows that a tangential velocity is weakly damped by increasing radiative flux and this behaviour is sustained at all locations from the wall (cone surface) to the edge of the boundary layer (free stream). Tangential flow is therefore strongest for the purely conductive heat transfer case ($R = 0$). Fig. 9c reveals that a very strong enhancement in temperature is produced with increasing R values. Thermal boundary layer thickness is therefore also elevated with stronger radiative flux in the coating regime. A homogenous effect on the temperature evolution is observed which is characteristic of the Rosseland diffusion flux model. Radiative equilibrium is achieved, and radiation acts purely diffusively with source terms due to emission. However, this model is restricted to gray fluent media and very high optical thicknesses. Nevertheless, it is evident that temperature augmentation is captured which is not possible when radiative effects are ignored in the mathematical model. While a simple algebraic model, Rosseland's model does provide a reasonable estimate of high temperature radiative behaviour. For more refinement multi-flux models are needed such as the two-flux model or Chandrasekhar discrete ordinates model (DOM) which can also accommodate specular radiation and transmittivity and reflectivity of the cone surface (wall). These approaches are under consideration for future investigations.

Table 2 presents the influence of selected parameters on axial and tangential skin frictions (C_{fx} and C_{gx}) and Nusselt number (Nu), along with a variation in the stream wise coordinate values, ξ. Both the cone vertex (lower stagnation point, ξ=0 and a general point downstream of the vertex along the cone surface are considered i. e. $\xi=1$). An increase in tangent hyperbolic power law index (n) is found to suppress the axial skin friction, has no influence on tangential skin friction and elevates Nusselt number at the cone vertex. At $\xi=1$, larger n values i. e. stronger shear-thinning characteristic of the magnetic polymer, again decreases axial skin friction, but elevates tangential skin friction and reduces Nusselt number. The location along the cone i. e. streamwise coordinate therefore exerts a role in how the shear-thinning non-Newtonian behaviour influences the axial flow. At ξ=0, increasing Weissenberg number, We, increases axial skin friction, has no influences on tangential skin friction but strongly reduces Nusselt number. Further along the cone surface at $\xi=1$, an increment in Weissenberg number, We, conversely decreases axial skin friction but enhances tangential skin friction and again suppresses Nusselt number. At the cone vertex, ξ=0, an increment in magnetic interaction parameter (M) exerts no tangible influence on axial or tangential skin friction or Nusselt number (although only tangential skin friction has zero magnitude). At $\xi=1$, however a very strong depletion in all three surface gradients is computed with larger magnetic interaction parameter indicating a suppression in both axial and tangential flow and a net reduction in heat transferred to the cone surface. Increasing Darcy parameter (Da) also induces no variation in axial or tangential skin friction or Nusselt number at ξ=0. However, further along the cone at $\xi=1$, larger Da values i. e. greater permeability boosts the axial skin friction component, decreases tangential skin friction and elevates Nusselt numbers. Increasing Forchheimer parameter (Fs) again has no impact at the cone vertex ξ=0 on axial or tangential skin friction or Nusselt number at. However, further along the cone at $\xi=1$, larger Fs values i. e. greater second order inertial drag decreases axial and tangential skin friction components and also reduces the Nusselt numbers. Increasing Rosseland radiative parameter (R) at the cone vertex ξ=0, strongly enhances axial skin friction, has no impact on circumferential skin friction (it is always zero at the cone vertex irrespective of whatever parameter is varied) and enhances significantly Nusselt number. Further along the cone at $\xi=1$, larger R values i. e. stronger thermal radiation, again increases axial skin friction and Nusselt number but suppresses tangential skin friction. With increasing Prandtl number (i. e. decreasing thermal conductivity of the magnetic polymer), at the cone vertex $\xi=0$, axial skin friction is elevated, no change arises in circumferential (tangential) skin friction and Nusselt number is also boosted. Further along the cone at $\xi=1$, a much stronger enhancement in axial skin friction and Nusselt number is induced whereas tangential skin friction is very strongly depleted. Finally, an increment in non-isothermal power-law index (m), strongly reduces axial skin friction, has no effect on tangential skin friction and significantly elevates Nusselt number, at the cone vertex, $\xi=0$. At $\xi=1$, again axial skin friction is reduced and Nusselt number is enhanced; however, there is also a substantial boost in tangential skin friction.

5.CONCLUSIONS

To simulate high temperature multi-physical rotational boundary layer coating flow, a detailed mathematical model has been developed to investigate the effects of thermal radiative flux on steady laminar convection boundary layer flow and heat transfer in magnetized tangent hyperbolic non-Newtonian coating flow external to a spinning cone with power-law variation in wall (cone surface) temperature, adjacent to a non-Darcian porous medium, under radial magnetic field. The Brinkman-Darcy-Forchheimer model is deployed for the porous medium which is assumed to be isotopic and homogenous. Rosseland's diffusion flux approximation is employed for the radiative heat transfer. The transformed non-dimensional conservation equations are solved numerically subject to physically appropriate boundary conditions using a second-order accurate implicit finite-difference Keller Box method. The numerical code is validated with previous studies. Comprehensive graphs are presented for the impact of Rosseland radiative number, Darcy number, Forchheimer number (non-Darcy inertial parameter), magnetic interaction parameter, tangent-hyperbolic non-Newtonian power-law index, non-isothermal power law index and Weissenberg (non-Newtonian) number of axial, tangential velocity components and temperature distributions with is included. Additionally, axial and tangential (circumferential) skin friction and Nusselt number values are tabulated for variation in selected key control parameters. The principal findings of the present analysis can be summarized as follows:

(i) An increment in Darcy parameter (Da) produces strong axial flow acceleration near the the cone surface (due to larger permeability), and also enhances significantly the tangential velocity; however, it considerably suppresses temperatures throughout the boundary layer transverse to the wall.

(ii) Further from the cone vertex, larger *Da* values enhance the axial skin friction component, decrease tangential skin friction and elevate Nusselt numbers.

(iii) Increasing Forchheimer parameter (*Fs*) further along the cone i. e. greater second order inertial drag decreases both axial and tangential skin friction components and also reduces the Nusselt numbers.

(iv) Increasing Rosseland radiative parameter (*R*) at the cone vertex ξ=0, strongly enhances axial skin friction, has no impact on circumferential skin friction and enhances significantly Nusselt number. Further along the cone at $\xi=1$, larger *R* values i. e. stronger radiative heat transfer, again increases axial skin friction and Nusselt number (i. e. boosts heat transfer to the cone surface) but suppresses tangential skin friction.

(v) Increasing non-isothermal power-law index (*m*), strongly reduces axial skin friction, has no effect on tangential skin friction and significantly increases Nusselt number, at the cone vertex, ξ=0. At $\xi=1$, again axial skin friction is also reduced and Nusselt number is again enhanced, although there is also a substantial elevation in tangential skin friction.

(vi) Increasing Weissenberg number decelerates axial flow and tangential flow whereas it boosts the temperature and thermal boundary layer thickness.

(vii) Elevation in non-Newtonian tangent hyperbolic index (*n*), elevates the pseudo-plasticity (shear-thinning) of the magnetic polymer and increases axial velocity magnitudes closer to the cone surface but suppresses tangential velocity and elevates temperature and thermal boundary layer thickness.

(viii) An increment in magnetic interaction parameter *M*, damps the axial flow, in particular in the vicinity of the cone surface, and pushes peak velocity further from the cone surface. Larger *M* values also strongly damp the tangential flow but significantly elevate temperature (due to work expenditure as heat in dragging the magnetic polymer against the action of the radial magnetic field) and also thermal boundary layer thickness.

The present study has shown the exceptional versatility of the Keller box finite difference method in accommodating two-parameter nonlinear multi-physical boundary layer flows in smart rotational coating systems. Future investigations may consider more complex radiative heat transfer flux models e. g. Traugott's P1-radiative differential approximation [67] and convective mass transfer (species diffusion) and anisotropic porous media [68]. Studies along these directions are underway and will be communicated imminently.

ACKNOWLEDGMENTS

The authors are grateful to both reviewers for their comments which have served to improve the present work.

FUNDING

No funding was received for this work.

REFERENCES

[1] J. Roegiers and S. Denys, CFD-modelling of activated carbon fibers for indoor air purification, *Chemical Engineering Journal*, 365, 80-87 (2019).

[2] W. Yuan *et al.*, Influence of porous media coatings on flow characteristics and vortex-induced vibration of circular cylinders, *Journal of Fluids and Structures*, 106, 103365 (2021).

[3] X. Ding *et al.*, Review on penetration and transport phenomena in porous media during slot die coating, *J. Polymer Science: Part B- Polymer Physics*, 55 (22), 1669-1680 (2017).

[4] Bhattacharya, A., Calmidi, V. V. and Mahajan, R. L., Thermophysical properties of high porosity metal foams, *International J. Heat Mass Transfer*, 45, 1017–1031 (2002).

[5] Bağci, Ö., Özdemir, M. and Dukhan, N. Flow regimes in packed beds of spheres from pre-Darcy to turbulent, *Transport in Porous Media*, 104(3), 501–520 (2014).

[6] Darcy, H., *Les Fontaines Publiques de la Ville de Dijon. 1st Ed.*, V. Dalmont Publishers. Paris, France (1856).

[7] Ghanbarian, B. *et al.*, Tortuosity in porous media: a critical review', *Soil Science Society of America Journal*, 77(5), 1461 (2013).

[8] Iversen, N. and Jørgensen, B. B., Diffusion coefficients of sulfate and methane in marine sediments: influence of porosity, *Geochimica et Cosmochimica Acta*, 57(3), pp. 571–578 (1993).

[9] H. Zhang *et al.*, Investigation of the redox behavior of biochar-based bipolar electrochemistry in porous media, *Chemical Engineering Journal*, 470, 144384 (2023).

[10] Jaganathan, S., Vahedi Tafreshi, H. and Pourdeyhimi, B., A realistic approach for modeling permeability of fibrous media: 3-d imaging coupled with CFD Simulation', *Chemical Engineering Science*, 63(1), pp. 244–252 (2008).

[11] Adler, P. M., Jacquin, C. G. and Quiblier, J. A., Flow in Simulated Porous Media', *International Journal of Multiphase Flow*, 16(4), pp. 691–712 (1990).

[12] G. A. Gómez-Ramos, Assessment of hydrodynamics in a novel bench-scale wall-cooled packed bioreactor under abiotic conditions, *Chemical Engineering Journal*, 375, 121945 (2019).

[13] Mohanty, D., Mahanta, G., Byeon, Haewon, Vignesh, S., Shaw, S., Khan, M. Ijaz, Abduvalieva, Dilsora, Govindan, Vediyappan, Awwad, Fuad A. and Ismail, Emad A. A., Thermo-solutal Marangoni convective Darcy-Forchheimer bio-hybrid nanofluid flow over a permeable disk with activation energy: Analysis of interfacial nanolayer thickness, *Open Physics*, vol. 21, no. 1, 2023, pp. 20230119. https://doi.org/10.1515/phys-2023-0119.

[14] D. Mohanty, N. Sethy, G. Mahanta, S. Shaw, Impact of the interfacial nanolayer on Marangoni convective Darcy-Forchheimer hybrid nanofluid flow over an infinite porous disk with Cattaneo-Christov heat flux, *Thermal Science and Engineering Progress*, 41, 101854, 2023. https://doi.org/10.1016/j.tsep.2023.101854

[15] K. Venkatadri, H. F. Öztop, V. R. Prasad, S. Parthiban and O. A. Bég, RSM-based sensitivity analysis of hybrid nanofluid in an enclosure filled with non-Darcy porous medium by using LBM method, *Numerical Heat Transfer, Part A: Applications* (2023). DOI: 10.1080/10407782.2023.2193708

[16] D. Mohanty, G. Mahanta, Ali Chamkha, S. Shaw, Numerical analyisis of interfacial nanolayer thickness on Darcy-Forchheimer Casson hybrid nanofluid flow over a moving needle with Cattaneo-Christov dual flux, *Numerical Heat Transfer, Part A: Applications*, DOI: 10.1080/10407782.2023.2263906

[17] D. Mohanty, G. Mahanta, S. Shaw, Analysis of irreversibility for 3-D MHD convective Darcy–Forchheimer Casson hybrid nanofluid flow due to a rotating disk with Cattaneo–Christov heat flux, Joule heating, and nonlinear thermal radiation, Numerical Heat Transfer, Part B: Fundamentals, 84:2, 115-142, DOI: 10.1080/10407790.2023.2189644.

[18] O. Anwar Bég, H S Takhar, R Bhargava, S Rawat and V R Prasad, Numerical study of heat transfer of a third-grade viscoelastic fluid in non-Darcy porous media with thermophysical effects, *Physica Scripta*, 77 065402 (2008).

[19] R. Naveen Kumar, R. J. Punith Gowda, B. J. Gireesha and B. C. Prasannakumara, Non-Newtonian hybrid nanofluid flow over vertically upward/downward moving rotating disk in a Darcy–Forchheimer porous medium, *European Physical Journal Plus*, 230, 1227–1237, (2021).

[20] H. Saleh *et al.*, Rotation effects on non-Darcy convection in an enclosure filled with porous medium, *International Communications in Heat and Mass Transfer*, 43, 105-111 (2013).

[21] J. C. Umavathi and O. Anwar Bég, Computation of von Karman thermo-solutal swirling flow of a nanofuid over a rotating disk to a non-Darcian porous medium with hydrodynamic/ thermal slip, *Journal of Thermal Analysis and Calorimetry*, 147:8445–8460 (2022).

[22] O. Anwar Bég, M.J. Uddin, T. Bég, R. Reddy Gorla, Numerical simulation of self-similar thermal convection from a spinning cone in anisotropic porous medium, *J. Hydrodynamics Series B,* 28 (2):184-194 (2016). DOI: 10.1016/S1001-6058(16)60620-0.

[23] Michael F. Modest, Sandip Mazumder, *Radiative Heat Transfer*, 4th Edition, Academic Press, New York, USA (2021).

[24] Flamant, Quentin, and David R.Clarke. Opportunities for minimizing radiative heat transfer in future thermal and environmental barrier coatings. *Scripta Materialia*, 173, 26-31 (2019).

[25] L. A. Castillo *et al.*, Methodology for the fast direct estimation of spectral radiative transport properties in microalgae photobioreactors, *Chemical Engineering Journal*, 458, 141462 (2023).

[26] L. Du *et al.*, Highly efficient subambient all-day passive radiative cooling textiles with optically responsive MgO embedded in porous cellulose acetate polymer, *Chemical Engineering Journal,* 469, 143765 (2023).

[27] C. Kim, N. Lior, A numerical analysis of NO_x formation and control in radiatively/conductively stabilized pulverized coal combustors, *Chemical Engineering Journal,* 71, 221-231 (1998).

[28] Y. Liu *et al.*, Reversible thermochromic and heat storage coating for adaptive de/anti-icing and thermal regulation, *Chemical Engineering Journal*, 482, 148837 (2024).

[29] K. Venkatadri, O. Anwar Bég, P. Rajarajeswari, V. Ramachandra Prasad, A. Subbarao and B. Md. Hidayathulla Khan, Numerical simulation and energy flux vector visualization of radiative-convection heat transfer in a porous triangular enclosure, *J. Porous Media*, 23(12):1–13 (2020) (13 pages).

[30] Mohanty, D., Mahanta, G., Shaw, S. *et al.* Thermal and irreversibility analysis on Cattaneo–Christov heat flux-based unsteady hybrid nanofluid flow over a spinning sphere with interfacial nanolayer mechanism. *J Therm Anal Calorim* 148, 12269–12284 (2023). https://doi.org/10.1007/s10973-023-12464-y

[31] M.K. Sarangi, D.N. Thatoi, Sachin Shaw, M. Azam, Ali J. Chamkha, M.K. Nayak, Hydrothermal behaviour and irreversibility ananlysis of Bodewadt flow of radiative and dissipative ternary composite nanomaterial due to a stretched rotating disk, *Materials Science and Engineering: B,*287, 116124, 2023. https://doi.org/10.1016/j.mseb.2022.116124

[32] Debashis Mohanty, Ganeswar Mahanta, Sachin Shaw, Irreversibility and thermal performance of nonlinear radiative cross-ternary hybrid nanofluid flow about a stretching cylinder with industrial applications, *Powder Technology,* 433, 119255, (2024). https://doi.org/10.1016/j.powtec.2023.119255

[33] Hartmann, J., Theory of the laminar flow of an electrically conductive liquid in a homogeneous magnetic field. *Mathematisk-fysiske Meddelelser,* 15(6) (1937).

[34] V. C. A. Ferraro and C. Plumpton, *An Introduction to Magneto-fluid Mechanics,* Oxford University Press, USA (1961).

[35] R. P. Chhabra, J.F. Richardson, *Non-Newtonian Flow and Applied Rheology: Engineering Applications,* 2nd Edition, Elsevier, USA (2008).

[36] Ying, A. Y. and A. A. Gaizer (1995). The effects of imperfect insulator coatings on MHD and heat transfer in rectangular ducts. *Fusion Engineering and Design*. 27, 634-641 (1995).

[37] Thess, A., E. V. Votyakov, and Y. Kolesnikov, Lorentz force velocimetry. *Phys. Rev. Lett.* 96, 1-10 (2006).

[38] A. Ghailane *et al.,* The effect of magnetic field configuration on structural and mechanical properties of TiN coatings deposited by HiPIMS and dcMS, *Surface and Coatings Technology*, 404, 126572 (2020).

[39] Z. Bi *et al.*, Multifunctional self-healing coatings with orderly distributed microcapsules aligned by magnetic field, *Chemical Engineering Journal*, 450, 138250 (2022).

[40] Y. Yu *et al.,* The effect of magnetic fields on the electroless deposition of Co–W–P film, *Surface and Coatings Technology*, 204, 2669-2676 (2010).

[41] A. Jung et al., Experiments, modeling and simulation of the magnetic behavior of inhomogeneously coated nickel/aluminum hybrid foams, *Journal of Magnetism and Magnetic Materials,* 378, 178-185 (2015).

[42] H. Matsushima, Effects of magnetic fields on iron electrodeposition, *Surface and Coatings Technology,* 179, 245-251 (2004).

[43] O. Anwar Bég, M. Ferdows, Tasveer A. Bég, T. Ahmed, M. Wahiduzzaman, Md. M. Alam, Radiative optically-dense magnetized transient reactive transport phenomena with cross diffusion and dissipation effects: *numerical simulations, J. Taiwan Inst. Chemical Engineers,* 66, 12–26 (2016).

[45] T. Thumma, O. Anwar Bég and Siva Reddy Sheri, Finite element computation of magnetohydrodynamic nanofluid convection from an oscillating inclined plate with radiative flux, heat source and variable temperature effects, *Proc. IMechE- Part N– J. Nanoengineering Nanomaterials and Nanosystems,* 231, (4) 179-194 (2017).

[46] V.R. Prasad, B. Vasu and O. Anwar Bég, Thermo-diffusion and diffusion-thermo effects on MHD free convection flow past a vertical porous plate embedded in a non-Darcian porous medium, *Chemical Engineering Journal*, 173, 598-606 (2011).

[47] F.C. Carreri *et al.,* HIPIMS ITO films from a rotating cylindrical cathode, *Surface and Coatings Technology*, 290, 65-72 (2016).

[48] J. Moreira *et al.,* Spin-coated freestanding films for biomedical applications, *Journal of Materials Chemistry B,* 18, 20-30 (2021).

[49] M. Kumari, G. Nath, Transient MHD rotating flow over a rotating sphere in the vicinity of the equator, *International Journal of Engineering Science*, 42, 1817-1829 (2004).

[50] F. T. Zohra, M.J. Uddin and A.I. Ismail, O. Anwar Bég and A. Kadir, Boundary layer anisotropic slip magneto-bioconvection flow from a rotating cone to a nanofluid with Stefan blowing effects, *Chinese J. Physics*, 56, 432-448 (2018).

[51] Shah, Z.; Bonyah, E.; Islam, S.; Gul, T. Impact of thermal radiation on electrical MHD rotating flow of Carbon nanotubes over a stretching sheet. *AIP Adv*. 9, 015115 (2019).

[52] Bég, O. Anwar, J. Zueco, S. K. Ghosh and A. Heidari, Unsteady magnetohydrodynamic heat transfer in a semi-infinite porous medium with thermal radiation flux: analytical and numerical study, *Advances in Numerical Analysis*, 2011, 1-17 (2011).

[53] P. Kumar and R. Nandkeolyar, Spectral simulation of hydromagnetic flow with dissipative and radiative heat transfer over an inclined rotating disk within a non-Darcy porous medium, *ZAMM*, 104 (2024). e202200395.

[54] Keller, H.B. & Cebeci, T. Accurate numerical methods for boundary layer flows 1. Two-dimensional flows *Proc. Int. Conf. Numerical Methods in Fluid Dynamics, Lecture Notes in Physics,* Springer, New York, USA (1971).

[55] P. Ramesh Reddy, S. Abdul Gaffar, B. Md. Hidayathulla Khan, K. Venkatadri and O. Anwar Bég, Mixed convection flows of tangent hyperbolic fluid past an isothermal wedge with entropy: A mathematical study, *Heat Transfer,* 50, 2895-2928 (2021).

[56] Abo-Eldahab EM and Elaziz MA. Hall current and ohmic heating effects on mixed convection boundary layer flow of a micropolar fluid from a rotating cone with power-law variation in surface temperature. *Int Commun Heat Mass Transfer*, 31: 751–762 (2004).

[57] V.R. Prasad, A. SubbaRao, N. Bhaskar Reddy, B. Vasu, O. Anwar Bég, Modelling laminar transport phenomena in a Casson rheological fluid from a horizontal circular cylinder with partial slip, *Proc IMechE- Part E: J. Process Mechanical Engineering, 227 (4) 309-326 (2013).*

[58] O. Anwar Bég, A. Subba Rao, N. Nagendra, CH. Amanulla, M. Surya Narayana Reddy and A. Kadir, Numerical study of hydromagnetic non-Newtonian nanofluid transport phenomena from a horizontal cylinder with thermal slip: aerospace nanomaterial enrobing simulation, *J. Nanofluids, Vol. 7, pp. 1–14 (2018).*

[59] S. Abdul Gaffar, V. Ramachandra Prasad, O. Anwar Bég, Md. H. Hidayathullah Khan and K. Venkatadri, Radiative and magnetohydrodynamics flow of third grade viscoelastic fluid past an isothermal inverted cone in the presence of heat generation/absorption, *J. Brazilian Soc. Mech Sci. Eng.* 40:127-146 (2018).

[60] S. A. Gaffar, V. R. Prasad, B. R. Kumar and O. Anwar Bég, Computational modelling and solutions for mixed convection boundary layer flows of nanofluid from a non-isothermal wedge, *J. Nanofluids,* 7, 1–9 (2018).

[61] S. Abdul Gaffar, O. Anwar Bég, V. Ramachandra Prasad, B. Md. Hidayathulla Khan and Ali Kadir, Computation of Eyring-Powell micropolar convective boundary layer flow from an inverted non-isothermal cone: thermal polymer coating simulation, *Computational Thermal Sciences,* 12(4):329–344 (2020).

[62] S. Abdul Gaffar, Khalil-Ur-Rehman, B. Md. Hidayathullah Khan and O. Anwar Bég, Entropy generation in magnetohydrodynamic radiative non-Newtonian dissipative convection flow from an inclined plane: numerical study, *Nanoscience and Technology: An Int. J.,* 11, 1–30 (2020).

[63] A. Sumithra, R. Sivaraj, V. R. Prasad, O. Anwar Bég, Ho-Hon Leung, F. Kamalov, S. Kuharat and B.R. Kumar, Computation of inclined magnetic field, thermophoresis and Brownian motion effects on mixed convective electroconductive nanofluid flow in a rectangular porous enclosure with adiabatic walls and hot slits, *International Journal of Modern Physics B* (2024) 2450398 (30 pages) DOI: 10.1142/S0217979224503983 (30 pages).

[64] A. Sumithra, R. Sivaraj, V. Ramachandra Prasad, O. Anwar Bég, Ho-Hon Leung, F. Kamalov and S. Kuharat, Computational study of MHD mixed convective flow of Cu/Al_2O_3-water nanofluid in a porous rectangular cavity with slits, viscous heating, Joule dissipation and heat source/sink effects, *Waves Random Complex Media* (2023). DOI: 10.1080/17455030.2023.2168786 (34 pages).

[65] D. Anilkumar and S. Roy, Unsteady mixed convection flow on a rotating cone in a rotating fluid, *Applied Mathematics and Computation*, 155, 2, 545–561 (2004).

[66] E. M. Sparrow and R. D. Cess, Magnetohydrodynamic flow and heat transfer about a rotating disk, *ASME Journal of Applied Mechanics*, 29, 181–187 (1962).

[67] O. Anwar Bég, N. Ali, A. Zaman, Eemaan T. A. Bég and Ayesha Sohail, Computational modelling of heat transfer in annular porous medium solar energy absorber with a P1-radiative differential approximation, *J. Taiwan Inst. Chemical Eng.,* 66, 258-268 (2016).

[68] O. Anwar Bég, M.J. Uddin, Tasveer A. Bég, Ali Kadir, M Shamshuddin, M. Babaie. Numerical study of self-similar natural convection mass transfer from a rotating cone in anisotropic porous media with Stefan blowing and Navier slip, *Indian J. Physics,* 94, 863-877 (2020).